

# Internal Tide Reflection and Turbulent Mixing on the Continental Slope

JONATHAN D. NASH

*College of Oceanic and Atmospheric Sciences, Oregon State University, Corvallis, Oregon*

ERIC KUNZE

*Applied Physics Laboratory, University of Washington, Seattle, Washington*

JOHN M. TOOLE AND RAY W. SCHMITT

*Department of Physical Oceanography, Woods Hole Oceanographic Institution, Woods Hole, Massachusetts*

(Manuscript received 29 April 2003, in final form 5 November 2003)

## ABSTRACT

Observations of turbulence, internal waves, and subinertial flow were made over a steep, corrugated continental slope off Virginia during May–June 1998. At semidiurnal frequencies, a convergence of low-mode, onshore energy flux is approximately balanced by a divergence of high-wavenumber offshore energy flux. This conversion occurs in a region where the continental slope is nearly critical with respect to the semidiurnal tide. It is suggested that elevated near-bottom mixing ( $K_p \sim 10^{-3} \text{ m}^2 \text{ s}^{-1}$ ) observed offshore of the supercritical continental slope arises from the reflection of a remotely generated, low-mode,  $M_2$  internal tide. Based on the observed turbulent kinetic energy dissipation rate  $\epsilon$ , the high-wavenumber internal tide decays on time scales  $O(1 \text{ day})$ . No evidence for internal lee wave generation by flow over the slope's corrugations or internal tide generation at the shelf break was found at this site.

## 1. Introduction

As part of ongoing efforts to understand internal waves and turbulence in the vicinity of rough topography, a field program was undertaken over the corrugated Virginia continental slope in the Mid-Atlantic Bight during spring 1998. Rough topography has been implicated as a likely catalyst for enhanced mixing. Observations near seamounts (Kunze and Toole 1997; Toole et al. 1997; Lueck and Mudge 1997; Eriksen 1998), canyons (Carter and Gregg 2002), ridges (Althaus et al. 2003; Rudnick et al. 2003), continental slopes (Moum et al. 2002), straits (Wesson and Gregg 1994; Polzin et al. 1996; Ferron et al. 1998), and rough shelf topography (Nash and Moum 2001) suggest an increase in turbulent diffusivities by two to three orders of magnitude in these regions.

Several mechanisms can produce elevated internal wave and turbulence levels over rough topography. Subinertial flow over bottom roughness of wavenumber  $k_{\text{bathy}}$  can generate internal lee waves if  $f/k_{\text{bathy}} < U < N/k_{\text{bathy}}$  (Thorpe 1992; MacCready and Pawlak 2001). Barotropic tidal flows will generate internal waves if the frequency

$\omega \gg k_{\text{bathy}}U$  and lee waves/solibores if  $\omega < k_{\text{bathy}}U$  (Bell 1975; St. Laurent et al. 2003; Balmforth et al. 2002). Internal waves can transfer their energy to higher wavenumbers susceptible to breaking and turbulence if they critically reflect from a bottom of slope  $s$  comparable to their ray-path slope  $\alpha$  (Eriksen 1982, 1985; Thorpe 1987; Slinn and Riley 1996; Müller and Liu 2000a,b). Internal waves can also be scattered to high wavenumber by small-scale bottom roughness (Müller and Xu 1992; Thorpe 2001). Which process dominates will depend on their respective efficiencies given local environmental conditions.

Munk and Wunsch (1998) envisioned tides playing a key role in the global thermohaline circulation, with energy cascading from the surface tide to baroclinic waves and ultimately to turbulent dissipation and mixing (Rudnick et al. 2003). Recent attention has focused on the generation of internal tides by barotropic tides (Merrifield et al. 2001; Althaus et al. 2003; Pingree and New 1989, 1991; Gerkema 2001, 2002). While some of this generation has high vertical wavenumber (and associated strong vertical shear capable of producing local mixing), the bulk is low mode. For example, 67%–89% of the energy flux is carried by the first two modes over Mendocino Escarpment (Althaus et al. 2003); models (Merrifield and Holloway 2002) and observations (Kunze

*Corresponding author address:* Dr. Jonathan Nash, College of Oceanic and Atmospheric Sciences, Oregon State University, 104 COAS Admin Bldg., Corvallis, OR 97331.  
E-mail: nash@coas.oregonstate.edu

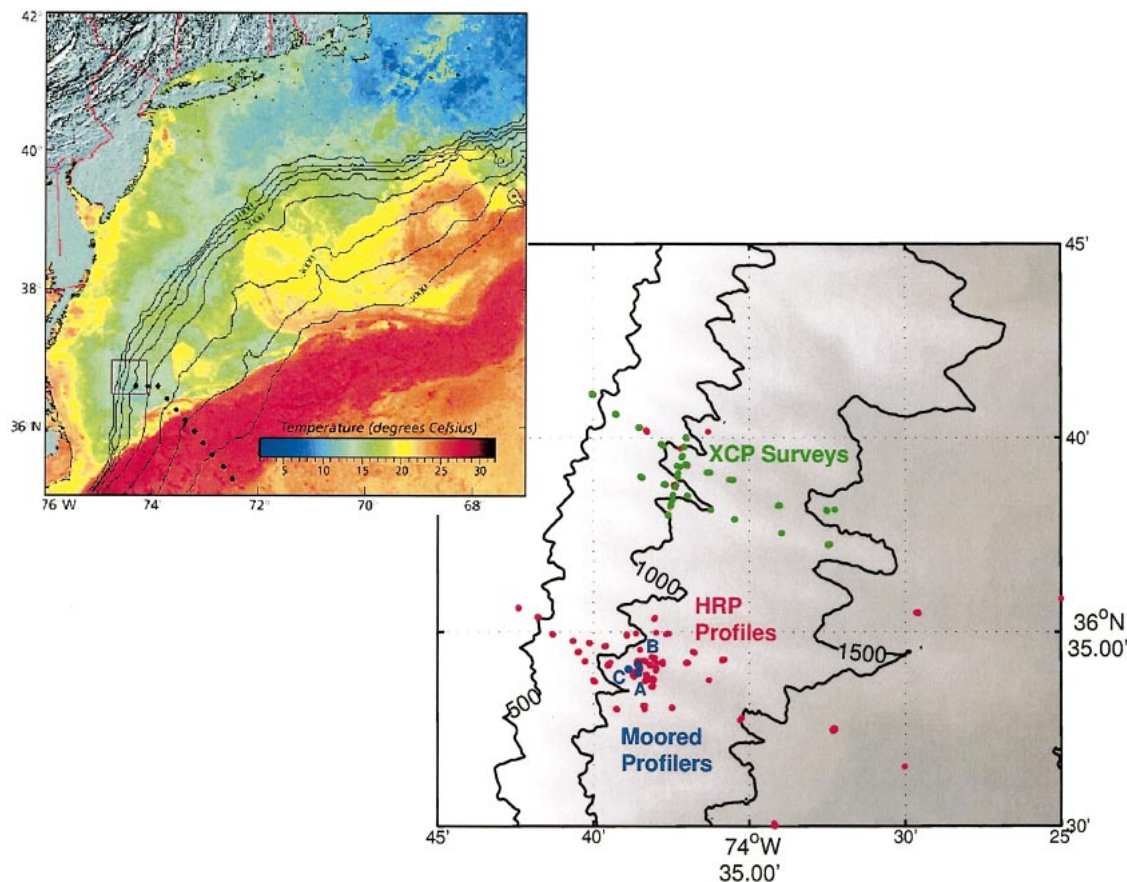


FIG. 1. The location of observations within the Mid-Atlantic Bight, relative the large-scale bathymetry and the Gulf Stream, as indicated by the SST overlay in the upper left. The location of the moored profilers (A, B, and C; blue), expendable current profiler (XCP) surveys (green), and High-Resolution Profiler (HRP) stations (red) are shown in the lower-right; additional stations crossing the Gulf Stream were occupied by HRP, as indicated in the upper-left panel. The bathymetry is shown by shading and contours at 500-m intervals.

et al. 2002b; Rudnick et al. 2003) indicate similar percentages radiating from the Hawaiian Ridge. Since the low modes have larger energy, larger group velocity, and weaker shear than their high-mode counterparts, they may propagate thousands of kilometers from their source before dissipating (Ray and Mitchum 1996; Cummins et al. 2001; St. Laurent and Garrett 2002). Likewise, turbulent losses in regions of internal tide generation appear to be weak. Althaus et al. (2003) found less than 2% of the internal tide generated over Mendocino Escarpment is dissipated at the escarpment. Small fractional losses to dissipation have also been observed over the sill at Knight Inlet (Klymak and Gregg 2004) and over the Hawaiian Ridge (Kunze et al. 2002b; Klymak et al. 2002). In contrast, Polzin (2004) infers more significant local losses in the broad field of rough topography on the Mid-Atlantic Ridge.

It is the eventual fate of these low-mode waves that is the concern of this paper, as such waves may transport momentum, dissipate energy, and produce mixing in regions far from their generation. Since many continental slopes are near- and supercritical with respect to

the semidiurnal tide (Cacchione et al. 2002), near-critical reflection is a possible dissipation mechanism. Communication of this sort complicates the parameterization of mixing in models if the associated nonlocal physics is neither recognized nor incorporated (e.g., Jayne and St. Laurent 2001; Sjöberg and Stigebrandt 1992).

The continental slope near Virginia is steep and corrugated by 200-m-high cross-isobath undulations of ~3-km wavelength between the 500- and 1500-m isobaths (Fig. 1). For typical summer stratification, the region between shelfbreak (~200 m) and 1000-m isobath is supercritical with respect to an  $M_2$  characteristic (average slope  $s = \Delta z/\Delta x \sim 0.2$ ; see Fig. 2). In the following, we present observations of turbulence, subinertial flow, and the internal-wave climate over this slope.

Our observations are organized in the following way. We motivate our analysis with the spatial distribution of turbulence in the water column and stratified bottom boundary layer (section 2a; Fig. 2). Raw observations are then presented of the winds, tides, sub- and superinertial time series, and frequency spectra (sections 2b–e). The discussion then focuses on the second half of

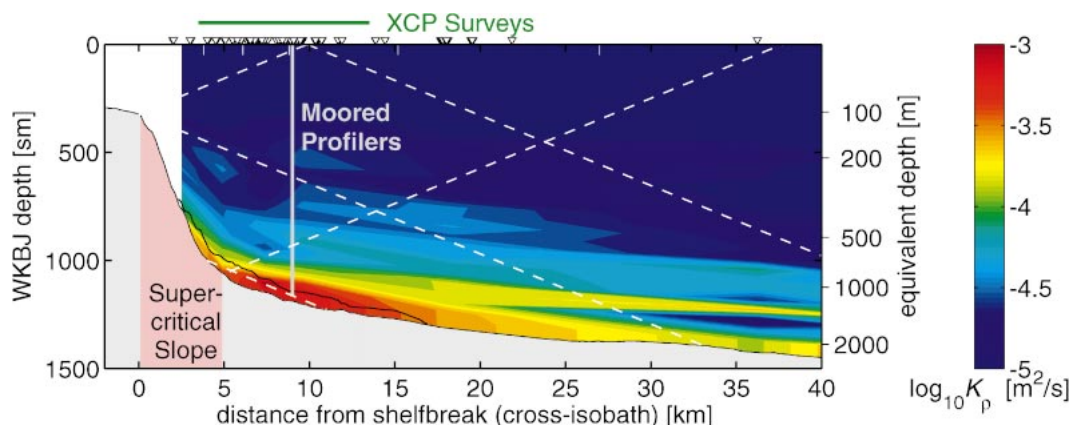


FIG. 2. Turbulent mixing ( $K_p \approx 0.2\epsilon N^{-2}$ ) derived from the HRP during the period 27 May–4 Jun. Several  $M_2$  internal tide characteristics are shown for reference. The region of supercritical topographic slope is also indicated (pink shading), as is the bathymetry through a gully (shading) and along its neighboring ridge (solid line). Data are plotted on a WKB-stretched grid in the vertical [units of stretched meters (sm); dimensional depths are indicated by the scale at right]. Data are from HRP profiles obtained within a 10-km along-isobath distance from the moored profiler array; profile locations are indicated with small triangles above the figure. Data were binned into six cross-isobath bins (delineated by white ticks) and 30 potential density levels prior to contouring.

the observation period when semidiurnal shear and energy fluxes were most intense and the expendable current profiler/expendable CTD (XCP/XCTD) surveys were conducted (section 2f). Observations of phase propagation and energy flux convergence during that time are presented, suggestive of a conversion of the low-mode tide into dissipative, high-wavenumber waves. A simple model assuming 2D wave reflection from an inclined plane is presented to support this interpretation (section 3).

## 2. Observations

An intensive set of field observations was obtained during May 1998 to investigate the internal wave and turbulence climates over a steep and corrugated continental slope in the outer Mid-Atlantic Bight off Virginia (Fig. 1). Three types of instrumentation were used to quantify different aspects of the flow field.

- 1) Fine- and microstructure observations were obtained using the High-Resolution Profiler (HRP; Schmitt et al. 1988), which acquired 245 profiles on the slope and along an offshore transect (to measure background levels).
- 2) The temporal evolution of barotropic and baroclinic flow structures was recorded using three moored profilers (MP; Doherty et al. 1999) separated by  $\sim 500$  m. The MP array was located in a gully (Fig. 1) at about the 1100-m isobath, just offshore of the transition from sub- to supercritical bottom slope (Fig. 2). Each profiler was deployed within a few days of the others, and collected data for 19-, 15.5-, and 16.5-day durations. They were recovered simultaneously. The MPs cycled along their mooring cables together, from 1100 m ( $\sim 15$  m above bottom) to 80 m, re-

turning one-way profiles every 1.5 h. Each profile took  $\sim 1$  h to collect.

- 3) Synoptic snapshots of the cross- and along-shelf internal wave activity were obtained using combined XCP/XCTD surveys (Sanford et al. 1993). Four spatial surveys at 3–4-h intervals provided surface-to-bottom velocity and density data along a nearby ridge crest, along its neighboring gully, and across the ridge–gully pair (Fig. 1; 25 stations per survey).

For this analysis, data from each of these sources has been rotated into a coordinate system aligned with the large-scale bathymetry (i.e., smoothed at 3 km to remove corrugations): along-isobath  $+y$  is defined to be  $18^\circ$  east of north and cross-isobath  $+x$  is  $18^\circ$  south of east. Wentzel–Kramers–Brillouin–Jeffreys (WKB) normalizations (Munk 1981; Althaus et al. 2003) are used to transform depths and perturbation fields to a constant- $N$  ocean. Vertical displacements ( $\xi_*$ , units of stretched meters  $\equiv$  sm) scale with stratification such that  $\xi_* \rightarrow \xi \sqrt{N(z)/N_o}$ , where  $N_o = 3.4 \times 10^{-3} \text{ s}^{-1}$  is the mean stratification. Velocity and pressure anomalies scale as  $(u'_*, p'_*) \rightarrow (u', p') \sqrt{N_o/N(z)}$ . Vertically integrated kinetic energy, potential energy, and energy flux are not altered by the coordinate transformation.

### a. Turbulence and mixing

While we anticipated strong internal lee wave generation in response to subinertial flows over the 200-m high topographic undulations ( $\sim 3$ -km alongslope wavelength), the near-bottom mean flow during the period when XCP surveys were conducted (27 May onward;  $u < 0.05 \text{ m s}^{-1}$ ) was too weak to generate waves (MacCready and Pawlak 2001; Thorpe 2001). Instead, we find the current and density structure consistent with

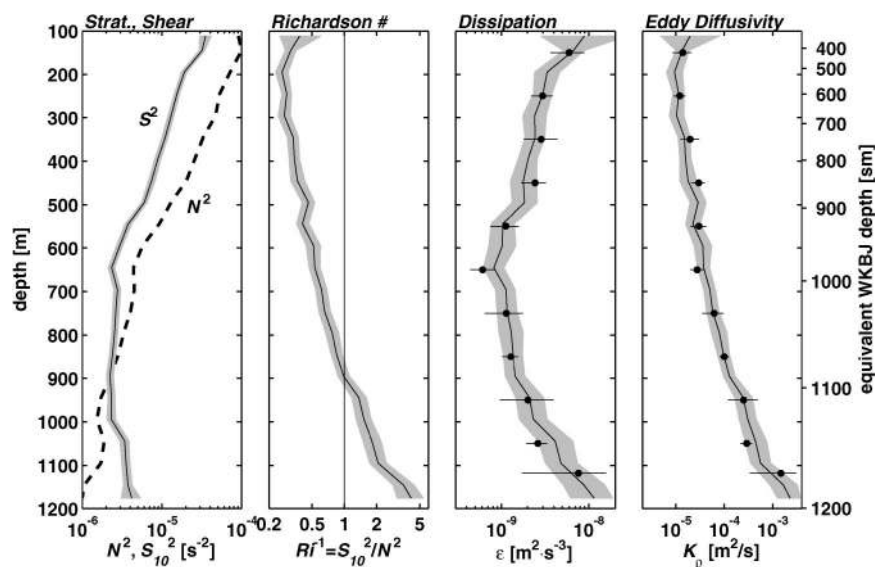


FIG. 3. Average vertical profiles of stratification ( $N^2$ ), 10-m shear ( $S_{10}^2$ ), 10-m inverse Richardson number, inferred turbulent energy dissipation rate ( $\epsilon$ ), and eddy diffusivity ( $K_p \approx 0.2\epsilon N^{-2}$ , Osborn 1980). Solid curves represent data from MP A during 27 May–4 Jun; dissipation rate was inferred from  $S_{10}^2$  and  $N^2$  using the Gregg–Henyey scaling. Symbols in the two rightmost panels represent dissipation rates derived from microscale shear variance measured by HRP’s two shear probes (Schmitt et al. 1988) with  $K_p$  referenced to the MP-derived average  $N^2$ ; each point represents a 100-m vertical average computed from 26 HRP profiles within a 10-km along-isobath distance from the MP array. Gray shading and error bars represent 95% bootstrap confidence limits on the mean.

along-isobath flow around rather than over the undulations. Internal lee waves were not observed judging by the absence of topographic horizontal scales in the overlying water column. Lee waves may have been generated prior to 27 May ( $u \sim 0.10 \text{ m s}^{-1}$ ), but these were not captured by our sampling.

Despite weak alongslope currents and the absence of lee waves, intense mixing was observed—primarily above regions with semidiurnally near- and subcritical bottom slopes at depths greater than 1000 m, as opposed to over the supercritical upper slope (Fig. 2). Numerical simulations by Legg (2004a,b) indicate that neither the cross- nor along-isobath barotropic tidal forcing is able to generate a high-wavenumber response where we observed elevated mixing. Rather, this region is in a “shadow zone” for locally generated internal tides (Legg 2004a), which tend to propagate above and along a semidiurnal characteristic emanating from the shelf break. A tide generated at the local shelf break would interact with the bottom more than 30 km from the shelf break where mixing is weak (Fig. 2).

### 1) SPATIAL DISTRIBUTION

The spatial structure of turbulent diffusivity  $K_p$  (Fig. 2) motivates the finescale analysis. In contrast to previous studies (Lueck and Mudge 1997; Lien and Gregg 2001), enhanced mixing is not observed along a semidiurnal characteristic emanating from the shelf break.

If shelf-generated internal tides were significant, then high-wavenumber baroclinic motions should propagate along such a characteristic (Prinsenberget al. 1974; Legg 2004a) with associated increases in energy density (Pingree and New 1989), shear, and mixing (Lueck and Mudge 1997; Lien and Gregg 2001). We observe no beams from the shelfbreak (in either baroclinic velocity, vertical displacement, energy flux, or dissipation), indicating that the shelfbreak-generated tide is weak, consistent with Legg (2004a).

Instead, turbulent diffusivities were enhanced by two orders of magnitude offshore of the supercritical slope in the bottom 100–500 m, in the shadow zone for a shelfbreak-generated internal tide (Legg 2004a). We hypothesize that internal-tide reflection near the 1000-m isobath is responsible for the elevated diffusivities.

Elevated levels of measured shear, inferred dissipation, and turbulent diffusivity are observed between the 1000- and 1200-m isobaths (Fig. 3). While shear scales roughly with stratification in the upper 600 m ( $S_{10}^2 \propto N^2$ ), this scaling does not hold within 500 m of the bottom. There,  $S_{10}^2$  increases, even though  $N^2$  decreases with depth. As a result, the average 10-m inverse Richardson number  $Ri^{-1} = S_{10}^2/N^2$  exceeds one in the bottom 300 m. Unstable  $Ri$  events likely drive the observed elevated turbulent energy dissipation and mixing.

The average vertical profile of turbulent dissipation rate based on shear and stratification from the moored profiler (using the Gregg–Henyey scaling; Gregg 1989)



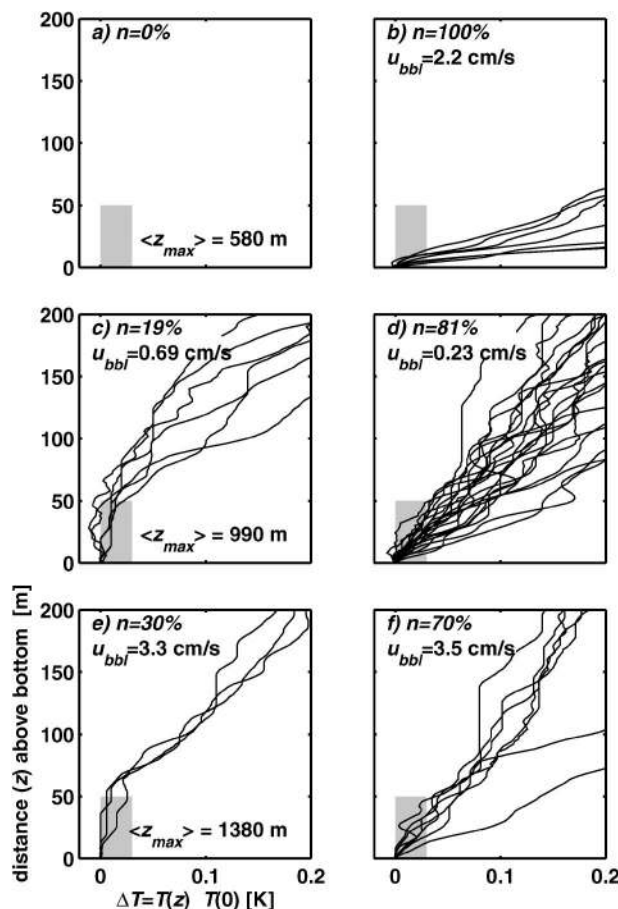


FIG. 4. Temperature structure in and above the bottom boundary layer. XCTD profiles obtained in similar water depths and with similar BBL thicknesses have been plotted together. Left panels [(a), (c), (e)] indicate profiles in which the BBL (as defined as  $\Delta T < 0.03$  K; gray shading) is at least 50-m thick; profiles at right [(b), (d), (f)] have thinner BBLs. Profiles obtained at water depths of (a), (b) 380–750 m; (c), (d) 810–1240 m and (e), (f) 1250–1530 m. The mean water depth is indicated as  $\langle z_{\max} \rangle$ . Also given in each panel are the percentage of profiles having similar BBL thickness, and the mean down-slope velocity in the bottom 20 m (positive offshore).

reproduces the direct turbulence measurements (Fig. 3). This suggests that (i) the HRP observations have adequately sampled the temporal intermittency of the mixing, (ii) the MPs have captured the shear associated with local turbulent production/dissipation, and (iii) the functional form and values of the constants in the Gregg–Heney scaling appropriately describe the relationship between internal wave intensity and dissipation rate near the slope.

## 2) BOTTOM BOUNDARY LAYER

Could the enhanced near-bottom mixing be associated with exceptionally thick bottom boundary layers? In this section, we investigate the structure of the near-bottom stratification and shear to determine if it is related to the observed pattern of dissipation.

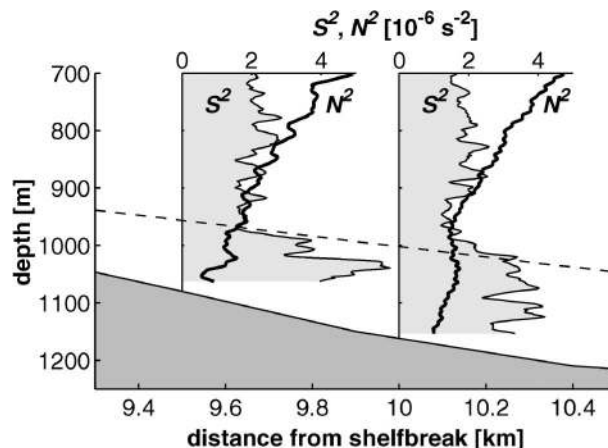


FIG. 5. Depth profiles of stratification (thick solid line) and 10-m shear variance at frequencies above  $0.8M_2$  (shading). Data are from 27 May–4 Jun at (left) MP C 9.5 km from shelf break and (right) MP A 10 km from shelf break. The dashed line indicates a semidiurnal characteristic which roughly bounds the extent of the high-shear bottom layer ( $Ri < 1/2$  on average; individual  $Ri$  estimates are much lower).

We use the quoted accuracy of the Sippican XCTD of  $\pm 0.03$  K to set the detection criterion of the bottom boundary layer (BBL). Fluid with  $\Delta T < 0.03$  K [ $\Delta T(z) = T(z) - T(0)$ , where  $T(0)$  represents the bottom temperature] is considered to be part of the well-mixed BBL. Profiles of relative temperature ( $\Delta T$ ) in the bottom 200 m are shown for three different regions of the slope: shallow (380–750 m) and supercritical (Figs. 4a,b), mid-depth (810–1240 m) and near-critical (Figs. 4c,d), and deep (1250–1530 m) and subcritical (Figs. 4e,f). Well-mixed BBLs exceeding 50 m in thickness were observed in only 18% of the XCP/XCTD profiles. On the steep supercritical slopes (water depths  $< 800$  m), mixed BBLs were not observed to exceed 10 m, and over the near-critical slopes in deeper locations only 20%–30% of the BBLs exceeded 50 m in thickness. No boundary layer thicker than 75 m was observed. In all cases, the mean near-bottom velocity is downslope. We observe little correlation between the BBL stratification (thickness or temperature anomaly) and the local velocity (along-isobath or cross-isobath magnitude or direction), either in a direct or a time-lagged sense.

These facts suggest that a classic, frictional boundary layer is not responsible for the elevated  $K_p$  and  $\epsilon$  that we observe ( $K_p > 10^{-4} \text{ m}^2 \text{ s}^{-1}$  within 300 m above the bottom). Instead, finescale shear is elevated for several hundred meters into the stratified water column (Figs. 3, 5). Average shear variance measured at the moored profilers in intrinsic frequencies  $0.8M_2$  and higher exceeds the stratification  $N^2$  within  $\sim 300$  m from the bottom. The layer of bottom-enhanced finescale shear appears to be approximately bounded above by an internal wave characteristic for the  $M_2$  tide (Fig. 5), not by the local stratification. Hence, we suspect the observed dis-

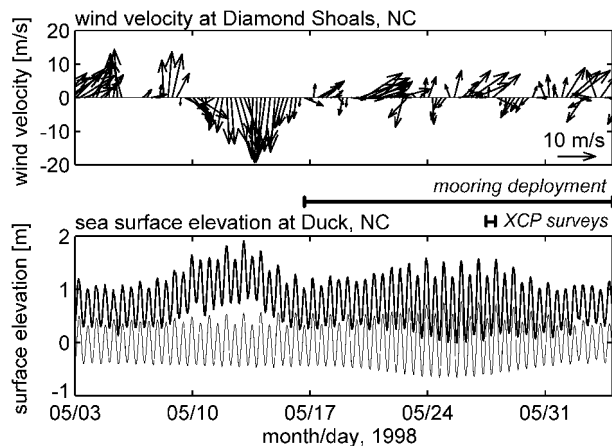


FIG. 6. Ten-meter winds at 35.15°N, 75.30°W (Diamond Shoals, NDBC station DSLN7, 150 km south of TWIST) and sea surface elevation at 36.18°N, 75.75°W (Duck Pier, NDBC station DUCN7; thick line). Predictions using TPXO.5 (Egbert 1997; thin line) give similar tidal amplitude and phase but do not include the response to atmospheric forcing during 9–15 May.

tribution of  $\epsilon$  is related to enhanced shear in the internal wave field, rather than classic bottom friction.

### b. Background variability

Strong northerlies (10–15 May) prior to the mooring deployments produced a 1-m rise in sea level along the coast, as evident in the time series of winds and sea surface elevation (Fig. 6). Following this storm, subinertial currents (estimated by convolving each time series with a 43.5-h Hanning window at each depth level) were southward at 15–20 cm s<sup>-1</sup> for ~1 week, subsiding to ~5 cm s<sup>-1</sup> for the remainder of the observation period (Fig. 7). The strong southward flow extends to within a few hundred meters of the bottom. In addition to these synoptic-time-scale changes, higher frequencies (~2-day period) are observed, with phase propagating upward from the bottom. Barotropic currents were generally alongslope and dominated by the subinertial flow. Reversals in the along-isobath current were observed in the bottom 100 m at the moorings (located in a gully). While suggestive of a topographic eddy, these features were too weak (<2 cm s<sup>-1</sup>) to be resolved by the spatial XCP surveys, and so we are not able to interpret them as persistent features.

Tidal forcing is predominantly semidiurnal, and the surface tide amplitudes agree well with modeled barotropic results (TPXO.5, Egbert 1997). Spring tides peaked on 25 May when amplitudes exceeded those of neap tides by ~50%. Barotropic tidal ellipse amplitudes (computed with TPXO.5, not shown) range from 1 cm s<sup>-1</sup> at the 1000-m isobath to 4 cm s<sup>-1</sup> at 200 m; variance ellipse major axes were aligned across isobaths with cross-isobath currents exceeding along-isobath by a factor of 2.

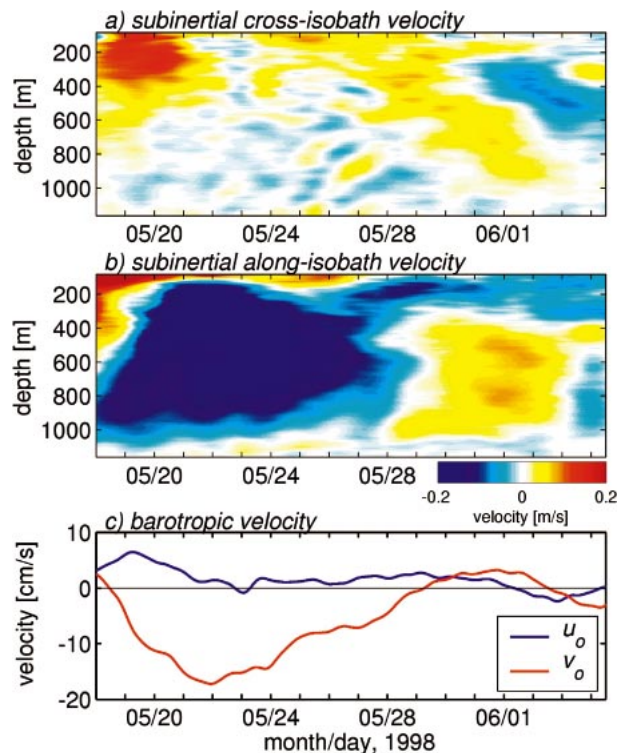


FIG. 7. Cross- ( $u_o$ ) and along- ( $v_o$ ) isobath components of (a), (b) baroclinic and (c) barotropic subinertial velocities from MP A.

### c. Energy flux $\langle \mathbf{u}'p' \rangle$

Estimates of the baroclinic energy flux are used to diagnose the dynamics of the internal wave field through energy budgets. The energy flux  $F_E = \langle \mathbf{u}'p' \rangle$  is the covariance of the wave-induced pressure  $p'$  and velocity  $\mathbf{u}'$ . By definition,  $p'$  and  $\mathbf{u}'$  are baroclinic fluctuations, and therefore have vanishing temporal and depth averages.

The perturbation pressure was determined following Kunze et al. (2002a). The density anomaly is estimated as  $\rho'(z, t) = \rho(z, t) - \bar{\rho}(z)$ , where  $\rho(z, t)$  is the instantaneous density and  $\bar{\rho}(z)$  is the time-mean vertical density profile, averaged over at least one wave period (>12.4 h). Alternatively,  $\rho'(z, t)$  may be defined in terms of the vertical displacement of an isopycnal  $\xi(z, t)$  so that  $\rho'(z, t) = (\bar{\rho}/g)\bar{N}^2\xi(z, t)$ . The pressure anomaly  $p'(z, t)$  is calculated from the density anomaly using the hydrostatic equation,

$$p'(z, t) = p_{\text{surf}}(t) + \int_z^0 \rho'(\hat{z}, t)g d\hat{z}. \quad (1)$$

Although the surface pressure  $p_{\text{surf}}(t)$  is not measured, it can be inferred from the baroclinicity condition that the depth-averaged pressure perturbation must vanish:

$$\frac{1}{H} \int_{-H}^0 p'(z, t) dz = 0. \quad (2)$$



For internal waves over a slope, we must also consider the contribution to  $\rho'$  from the barotropic tide's cross-isobath velocity (Baines 1982), which produces baroclinic vertical displacements. For no normal flow at the bottom (defined by  $z = -sx$ ), a barotropic tidal velocity  $u_{bt} = u_{bt}^o \cos(\omega_{M_2} t)$  induces a vertical velocity  $w_{bt} = -u_{bt}s$  at  $z = -H$  and a vertical velocity  $w_{bt}(z) = u_{bt}s(z/H)$  throughout the water column. The associated vertical displacement  $\xi_{bt}(t) = \int_0^t w_{bt}(t^*) dt^*$  is

$$\xi_{bt} = \xi_{bt}^o(z/H) \sin(\omega_{M_2} t), \quad (3)$$

where  $\xi_{bt}^o = u_{bt}^o s / \omega_{M_2}$  is the maximum vertical displacement. For bottom slopes and cross-isobath barotropic tidal velocities typical of the Virginia slope ( $s \sim 0.1$  and  $u_{bt}^o \sim 1 \text{ cm s}^{-1}$ ),  $\xi_{bt}^o \sim 7 \text{ m}$ . In comparison with the observed 20–100-m internal tide vertical displacements,  $\xi_{bt}$  is small. We nevertheless remove the barotropic-induced baroclinic pressure anomaly,  $p'_{bt} = \int_z^0 \bar{\rho} N^2 \xi_{bt}(\hat{z}, t) d\hat{z}$  at each station prior to computing internal wave energetics. For this calculation, the  $M_2$  across-isobath barotropic transport  $q_{bt}$  is spatially uniform and is used to compute  $u_{bt}$  as  $q_{bt}/H$ ; our XCP observations and the TPX0.5 model both yield consistent estimates ( $q_{bt}^o \approx 11 \text{ m}^2 \text{ s}^{-1}$ ).

The perturbation velocity is defined as

$$\mathbf{u}'(z, t) = \mathbf{u}(z, t) - \bar{\mathbf{u}}(z) - \bar{\mathbf{u}}_o(t), \quad (4)$$

where  $\mathbf{u}(z, t)$  is the instantaneous velocity,  $\bar{\mathbf{u}}(z)$  is the time-mean of that velocity, and  $\bar{\mathbf{u}}_o(t)$  determined by requiring baroclinicity:

$$\frac{1}{H} \int_{-H}^0 \mathbf{u}'(z, t) dz = 0. \quad (5)$$

Full-depth profiles of pressure or velocity were not available from the moored profilers, which did not sample the upper 80 m of the water column. It was therefore necessary to extrapolate  $u$  and  $p$  to the surface to determine  $\bar{\mathbf{u}}_o(t)$  and  $\bar{p}_o(t)$ . This was done by fitting the barotropic and first baroclinic mode to the available data. To estimate the error introduced by excluding the upper 80 m of data, we subsample the XCP/XCTD profiles, perform a mode fit to extrapolate the data, and then compare the computed energy flux with that calculated using the original full-depth profile. We find that the depth-integrated energy flux computed from partial-depth data underestimates  $|\int_{-H}^0 \langle \mathbf{u}' p' \rangle dz|$  by  $0.12 \text{ kW m}^{-1}$  on average and produces a  $0.20 \text{ kW m}^{-1}$  rms error. MP-derived estimates of  $\langle \mathbf{u}' p' \rangle$  should be regarded with caution. Flux estimates from the XCP/XCTD surveys are fully resolved in space, but lack temporal coverage. We thus combine both measurements to evaluate the internal wave climate.

Temporal averages  $[\bar{p}_*(z), \bar{\mathbf{u}}_*(z)]$  for the XCP/XCTD data were the means over four occupations at each station, generally spanning  $\sim 15 \text{ h}$ . These were used to determine the perturbation quantities and energy flux. The superinertial baroclinic fluctuations shown in Figs.

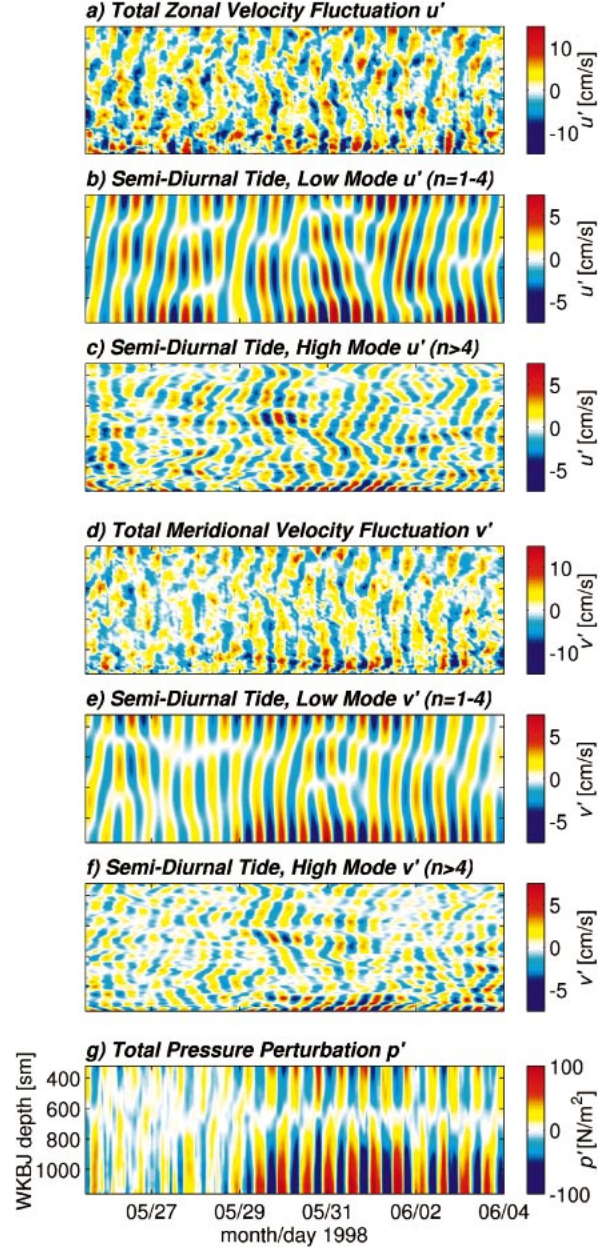


FIG. 8. Time series of (a)–(c) perturbation zonal velocity, (d)–(f) meridional velocity, and (g) the corresponding pressure perturbation during the latter half of MP A's deployment. Here, (a), (d), and (g) represent the full perturbation fields (periods less than 30 h, depth-mean removed), and (b), (c), (e), and (f) have been bandpass filtered for frequencies  $0.7 < \omega/\omega_{M_2} < 1.3$ . Fits to the first four vertical modes are presented in (b), (e); high-wavenumber residuals are shown in (c), (f). Pressure perturbations were derived from density data as described in the text.

8a, 8d, and 8g were used as perturbation quantities to compute energy fluxes for the moored profiler data.

Profiles of perturbation velocity and isopycnal displacement are also used to estimate the depth-averaged baroclinic horizontal kinetic energy density  $\text{HKE} = \langle u'^2 + v'^2 \rangle / 2$  and available potential energy density  $\text{APE} =$

$N^2\langle\xi^2\rangle/2$ . For a single propagating wave, HKE:APE is an intrinsic property of the wave, equal to  $(\omega^2 + f^2)/(\omega^2 - f^2) = 2.14$  for  $M_2$  at  $36.5^\circ\text{N}$ .

#### d. High-frequency variability

The subinertial variability (Fig. 7) was removed from the MP data to produce baroclinic records with near-inertial and higher frequency content. High-frequency time series, produced by modal decomposition and temporal filtering of the baroclinic velocity fields, are presented in Fig. 8. We decompose the vertical structure using WKBJ-stretched flat-bottom internal wave modes. While dynamically inappropriate for internal wave propagation on a slope, flat-bottom modes are useful for separating low and high vertical wavenumber contributions. In contrast, slope modes (Wunsch 1969) are dynamically relevant, but are ill-defined for near-critical bottom slopes. In addition, a single slope mode will represent a variety of physical wavenumbers and contain both shoreward and offshore energy propagation over a supercritical bottom, obscuring interpretation of the modal decomposition. In contrast, decomposition into flat-bottom modes isolates the energetics associated with a particular wavenumber without including the dynamical response of that wavenumber to the bottom within the mode description.

The first four stretched baroclinic modes were fit to WKBJ-stretched velocity data  $\mathbf{u}'$ , which was bandpass filtered between  $0.7$  and  $1.3 \omega_{M_2}$ , where  $\omega_{M_2}$  represents the  $M_2$  tidal frequency (12.4 h). We thus obtain a low-mode representation of the data:

$$u(n = 1-4) = \sum_{n=1-4} u_n(t)Z_n(z), \quad (6)$$

where  $u_n$  is the modal amplitude associated with the mode- $n$  vertical structure function,  $Z_n(z)$ . The high vertical wavenumber representation is simply the difference between the total and low-mode velocity, each bandpassed between  $0.7$  and  $1.3 \omega_{M_2}$ .

The pressure perturbation is predominantly first mode and of semidiurnal frequency, so only the raw  $p'$  is shown ( $p'$  has a redder vertical wavenumber spectrum than  $u'$  or  $\xi'$  by a factor of  $k_z^{-2}$  since pressure is related to the vertical integral of vertical displacement). As expected, the velocity and vertical displacement fluctuations have a much broader modal content—high-wavenumber velocity fluctuations are of similar magnitude to the low modes and are intensified near the bottom.

A clear transition in the character of the flow was observed on 29 May, when both velocity fluctuations and pressure perturbations increased dramatically. At the same time, the along-isobath barotropic current became negligible. These changes are also evident in frequency spectra of 10-m shear (Fig. 9). Prior to 29 May, shear was dominantly near- and subinertial. Afterward, the observed shear was dominantly semidiurnal. In the following, we focus on data from the final week of the

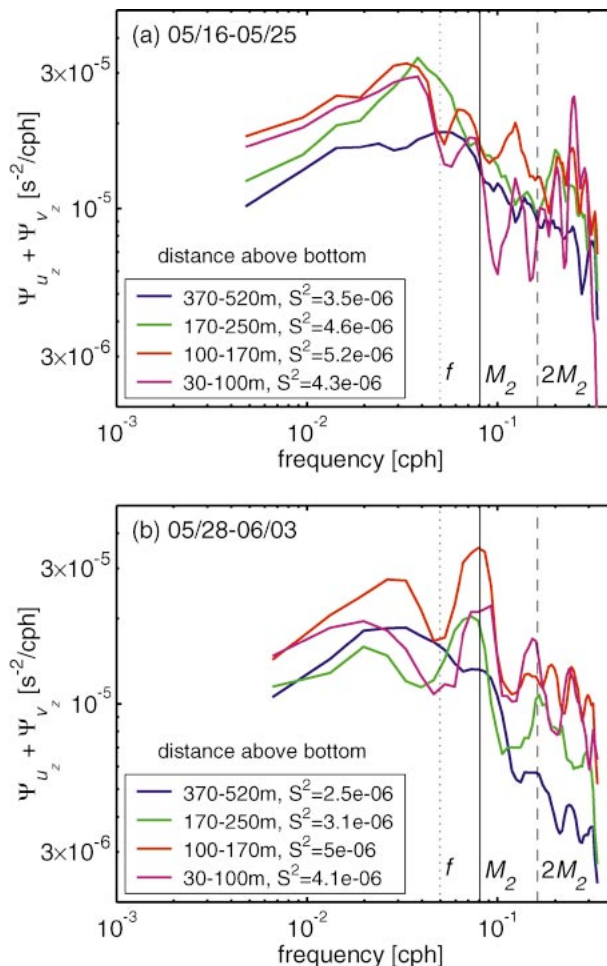


FIG. 9. Spectra of 10-m shear from MP A during (a) 16–25 May and (b) 28 May–3 Jun 1998 at four different heights above the bottom. During the first half of the deployment, near-bottom shear was dominated by subinertial frequencies; during the latter half, the spectra exhibit a strong peak at the  $M_2$  semidiurnal frequency, particularly in the bottom 200 m. For these plots, the individual profiles of  $du/dz$  and  $dv/dz$  were smoothed using a 10-m boxcar filter and gridded onto isopycnals to remove vertical Doppler-shifting ( $\sim k_z w$ ;  $k_z$  is vertical wavenumber and  $w$  is vertical velocity). Spectra of each component were independently computed on isopycnals, summed to produce the total shear spectrum ( $\Psi_{u_z} + \Psi_{v_z}$ ), and averaged over isopycnals occupying the indicated height-above-bottom ranges.

deployment (28 May–4 June 1998), because this was the time when XCP surveys (performed 27–29 May) captured the spatial structure of the strong semidiurnal shear (and energy flux).

Intensified semidiurnal shear became evident in the lower 100–200 sm (300–500 m) during 30 May–3 June (Fig. 9b). During that period, motions with 250–300-m vertical wavelengths,  $5\text{--}10 \text{ cm s}^{-1}$  amplitudes, and  $0.6\text{--}0.7 \text{ cm s}^{-1}$  upward phase velocity dominate the high-wavenumber time series (Figs. 8c,f). These waves are the source of the high shear shown in Fig. 5. We interpret these as high- $k_z$  waves of semidiurnal and higher intrinsic frequencies with downward energy propagation.



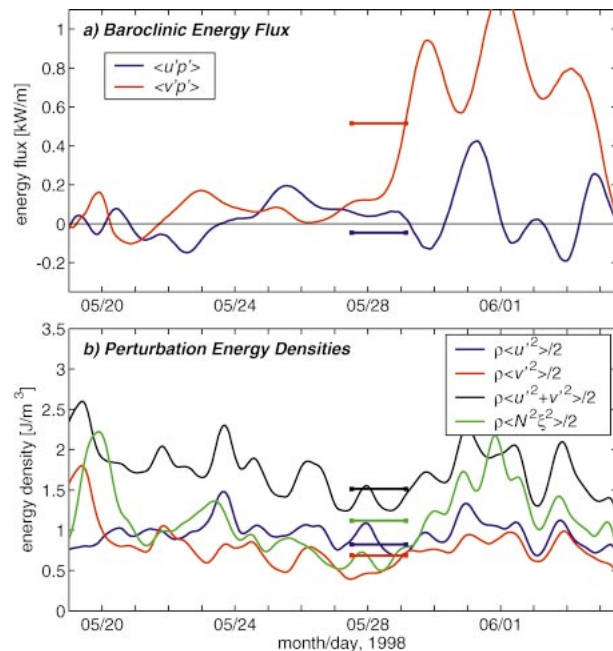


FIG. 10. Time evolution of (a) depth-integrated energy-flux and (b) depth-averaged baroclinic energy density computed from  $\mathbf{u}'$ ,  $p'$ , and  $\xi'$ . The smooth curves represent 1.5-h estimates from MP A, smoothed using a 22.5-h Hanning window, and depth-integrated (from 90 m to the bottom). Horizontal bars depict mean quantities computed from the XCP surveys 7–10 km north of the mooring. MP-derived energy fluxes are computed from mode-1 fits.

We believe the source for these waves to be inshore of the moorings due to near-critical reflection of an onshore-propagating low-mode internal tide, consistent with the semidiurnal characteristic shown in Fig. 5. Cross-isobath trends in the semidiurnal phase of the mode-1 amplitudes of  $u$ ,  $v$ , and  $p$ , as computed through harmonic analysis at each of the moorings (not shown) support this hypothesis. Low-mode phase at the offshore mooring leads that at the onshore mooring by  $\sim 30^\circ$  in  $u$ ,  $v$ , and  $\sim 10^\circ$  in  $p$ , suggesting onshore propagation. Harmonic analysis of the XCP records indicates similar phase shifts.

#### e. Time dependence

Significant temporal variability was observed in the depth-averaged energetics of the internal wave field (Fig. 10). Although near-inertial and higher-frequency variability is included in these estimates, the dominant contribution to the energy flux is from semidiurnal fluctuations. Most notable is the dramatic increase in the along-isobath energy-flux  $\langle v'p' \rangle$  on 29 May. The onset of  $1 \text{ kW m}^{-1}$  northward energy flux coincides with a relaxation of the  $\sim 10\text{--}15 \text{ cm s}^{-1}$  barotropic southward currents (Fig. 7c), an increase in perturbation potential energy density (as a result of semidiurnal vertical displacements; Figs. 8f and 10b), and a shift in frequency

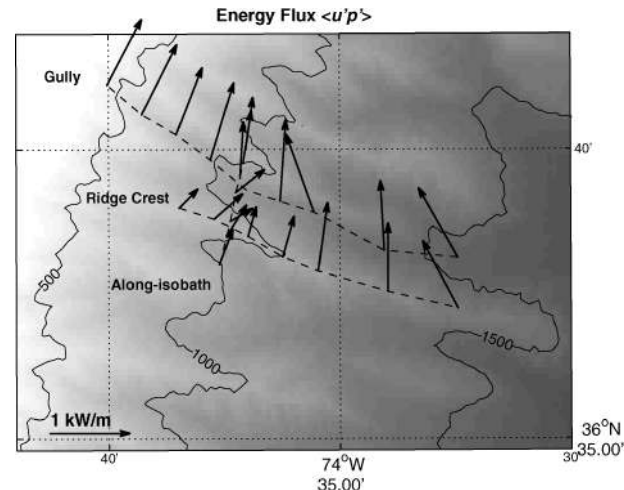


FIG. 11. Depth-integrated internal wave energy flux  $\int_{-H}^0 \langle \mathbf{u}'p' \rangle dz$  from XCP/XCTD surveys. Dashed lines indicate the XCP transects.

content of 10-m shear from sub- and near-inertial to semidiurnal (Fig. 9).

A decrease in HKE:APE from its semidiurnal value ( $\sim 2$ ) was observed along with the increase in energy flux after 29 May. We will show in section 3b that reduced HKE:APE near the boundary is a signature of a horizontally standing mode; in the limit of reflection from a vertical wall,  $\text{HKE}/\text{APE} \sim 0$  near the wall, an artifact of having significant vertical displacements yet no normal flow at the boundary. This suggests that horizontally standing modes in the cross-isobath direction may dominate the energetics during periods of high energy flux. This interpretation will be borne out by later analysis.

Velocity variance in the cross-isobath direction exceeds that of the along-isobath direction by  $\sim 25\%$  (Figs. 8 and 10b). The northward energy flux (Fig. 10a) is therefore not due to a single propagating internal wave, for which the ratio of along-to cross-isobath velocity variance should be  $\omega^2/f^2 \sim 2.78$ . Furthermore, the squared coherence,

$$\text{coh}_{vp}^2 = \frac{\langle v'p' \rangle^2}{\langle v'^2 \rangle \langle p'^2 \rangle}, \quad (7)$$

is very low:  $\text{coh}_{vp}^2 \sim 0.05$  before 29 May and  $\sim 0.16$  afterward (with a maximum  $\sim 0.33$  on 29–30 May). Thus, less than one-third of the velocity/pressure variance is associated with the net along-isobath energy flux on 29–30 May (Figs. 10 and 11). In the cross-isobath direction,  $\text{coh}_{up}^2 = 0.015$  throughout. These results suggest that the measured flux is not the product of a single propagating wave, for which  $\text{coh}^2 \sim 1$ . For reference, a coherence of 0.03 is significant at the 95% confidence level, assuming independence of 10-m data.

#### f. Energetics

Depth-integrated energy fluxes calculated from the XCP/XCTD surveys are generally along-isobath and

northward (Fig. 11). There is also a suggestion of cross-isobath convergence—in waters deeper than 1000 m, the flux is slightly upslope, while in shallow water, the flux is either along-isobath or downslope.

We illustrate this convergence in more detail with cross sections of energy flux (Fig. 12). The energy flux is decomposed by projecting the perturbation velocity ( $u'$ ,  $v'$ ) and pressure ( $p'$ ) onto the flat-bottom vertical-mode structure functions and computing the energy flux from those projections (6). This allows separation of low modes (which may propagate long distances) from high wavenumbers (which are presumed to be generated and dissipated locally because of their slow group velocities and susceptibility to nonlinearity). Cross sections of energy flux and inferred diffusivity are shown along the ridge crest (Figs. 12a–c) and in the gully (Figs. 12d–f). Vertical averages of the energy flux are shown above each plot (Figs. 12a', b', d', e').

Mode 1 is propagating onshore and its energy flux is converging (Figs. 12a,d). The high-wavenumber signal is dominated by a divergent beam of strong offshore energy flux near the bottom below 900 m (1100 sm; Figs. 12b,e). Such a beam may be formed through near-critical reflection from a supercritical linear slope (Eriksen 1982, 1985). The partitioning of energy flux may also be interpreted in terms of supercritical slope modes (2D modes in a supercritical wedge Wunsch 1969), for which a low- $k$  onshore energy flux is balanced by an intense high- $k$  offshore flux near the bottom.

In both of our ridge–crest and gully sections, the near-bottom beam (Figs. 12b,e) originates near the 900-m isobath and coincides with the near-bottom layer of elevated diffusivity (Figs. 12c,f). At the shoremost station, the high-wavenumber wave field is weak; inferred diffusivities are small ( $K_p \sim 10^{-5} \text{ m}^2 \text{ s}^{-1}$ ) and not bottom-intensified despite the similarly rough bottom. The two slope environments (ridge and gully) appear indistinguishable in terms of energy-flux convergence and diffusivity.

Ridge and gully sections each indicate low-mode convergence of similar magnitude to the high-wavenumber divergence in the lower water column. The average low-mode convergence [ridge:  $(-6 \pm 2) \times 10^{-8} \text{ W kg}^{-1}$ , gully:  $(-4 \pm 2) \times 10^{-8} \text{ W kg}^{-1}$ ] exceeds the high-wavenumber divergence [ridge:  $(3 \pm 3) \times 10^{-8} \text{ W kg}^{-1}$ , gully:  $(2 \pm 3) \times 10^{-8} \text{ W kg}^{-1}$ ], consistent with there being another sink for the converging cross-isobath energy flux, such as local turbulent dissipation  $\epsilon$  or the divergence of along-isobath energy flux.

To determine the most significant contributions in the internal wave energy budget, we consider the evolution of depth-averaged baroclinic energy  $E$ :

$$\frac{\partial E}{\partial t} + \nabla \cdot \langle \mathbf{u}' p' \rangle = -\epsilon + G, \quad (8)$$

where  $G$  is the baroclinic generation by the barotropic tide. The internal tide energy density increased during

the XCP surveys and cannot be ignored. From Fig. 10, the rate of change of baroclinic perturbation energy density was at most  $\partial E / \partial t = 1 \text{ (J m}^{-3}\text{) / day} = 1 \times 10^{-8} \text{ W kg}^{-1}$ .

The net energy-flux divergence  $\nabla \cdot \langle \mathbf{u}' p' \rangle$  is obtained with increased precision by including all vertical modes (low and high wavenumbers) as well as combining both ridge and gully transects of the depth-integrated energy flux prior to calculating its gradient (Fig. 13). Evaluated at the 1000-m isobath, there is a net convergence of cross-isobath energy flux:  $d\langle u' p' \rangle / dx = (-7 \pm 2) \times 10^{-8} \text{ W kg}^{-1}$ . The along-isobath flux-divergence is estimated by differencing the XCP- and MP-derived energy-flux, and is  $d\langle v' p' \rangle / dy = 0.3 \pm 0.2 \text{ W m}^{-2} / 10 \text{ km} = (3 \pm 2) \times 10^{-8} \text{ W kg}^{-1}$ . The net divergence is  $\nabla \cdot \langle \mathbf{u}' p' \rangle = (4 \pm 3) \times 10^{-8} \text{ W kg}^{-1}$ . In comparison, the observed dissipation rates were  $\epsilon \sim 0.5 \times 10^{-8} \text{ W kg}^{-1}$ .

We estimate the barotropic–baroclinic conversion term  $G$  from the simulations of Legg (2004a). In those simulations, an  $\sim 20 \text{ W m}^{-1}$  internal tide is generated for a  $0.01 \text{ m s}^{-1}$  deep baroclinic cross-isobath forcing, typical of the Virginia slope. Most of the baroclinic energy flux is generated at the shelf break, with less than 10% originating over the deeper slope. Assuming that generation occurs over 5 km of slope in 1000 m of water, the local generation is  $G = 2 \text{ W m}^{-1} / 1000 \text{ m} / 5000 \text{ m} = 0.04 \times 10^{-8} \text{ W kg}^{-1}$ . Hence it is reasonable to neglect local generation by the barotropic tide in (8).

In summary, the cross-isobath energy-flux convergence of  $(7 \pm 2) \times 10^{-8} \text{ W kg}^{-1}$  is the source term in (8), with both along-isobath divergence and turbulent dissipation being possible sinks. The net convergence  $\nabla \cdot \langle \mathbf{u}' p' \rangle = (4 \pm 4) \times 10^{-8} \text{ W kg}^{-1}$  is large enough to both supply the baroclinic energy density increase during 29–31 May (Fig. 10) and fuel the observed turbulence production rate of  $\epsilon \sim 0.5 \times 10^{-8} \text{ W kg}^{-1}$ . However, the uncertainties are sufficiently large that we cannot preclude other energy sources supporting the observed turbulence (Figs. 2, 3).

In any event, the high-wavenumber internal waves formed over the slope must dissipate somewhere. If the only means of attenuation were local turbulent dissipation of  $O(10^{-8} \text{ W kg}^{-1})$ , the offshore flux of high-wavenumber energy ( $\sim 1 \text{ W m}^{-2}$ ) could propagate about 100 km before dissipating and support mixing well into the ocean interior. Only 5%–10% of the  $O(1 \text{ kW m}^{-1})$  cross-isobath energy flux is dissipated locally by turbulence over the slope [i.e., the dissipation efficiency, as defined by St. Laurent et al. (2002), is 0.05–0.1]. Since much of the high- $k$  flux is directed offshore and downward (hugging the bottom), it may dissipate or scatter during interaction with the subcritical bottom away from our site of observations.

### 3. Interpretation

Our observations suggest the following.

- 1) Ten-meter shear during 28 May–3 June 1998 is dom-

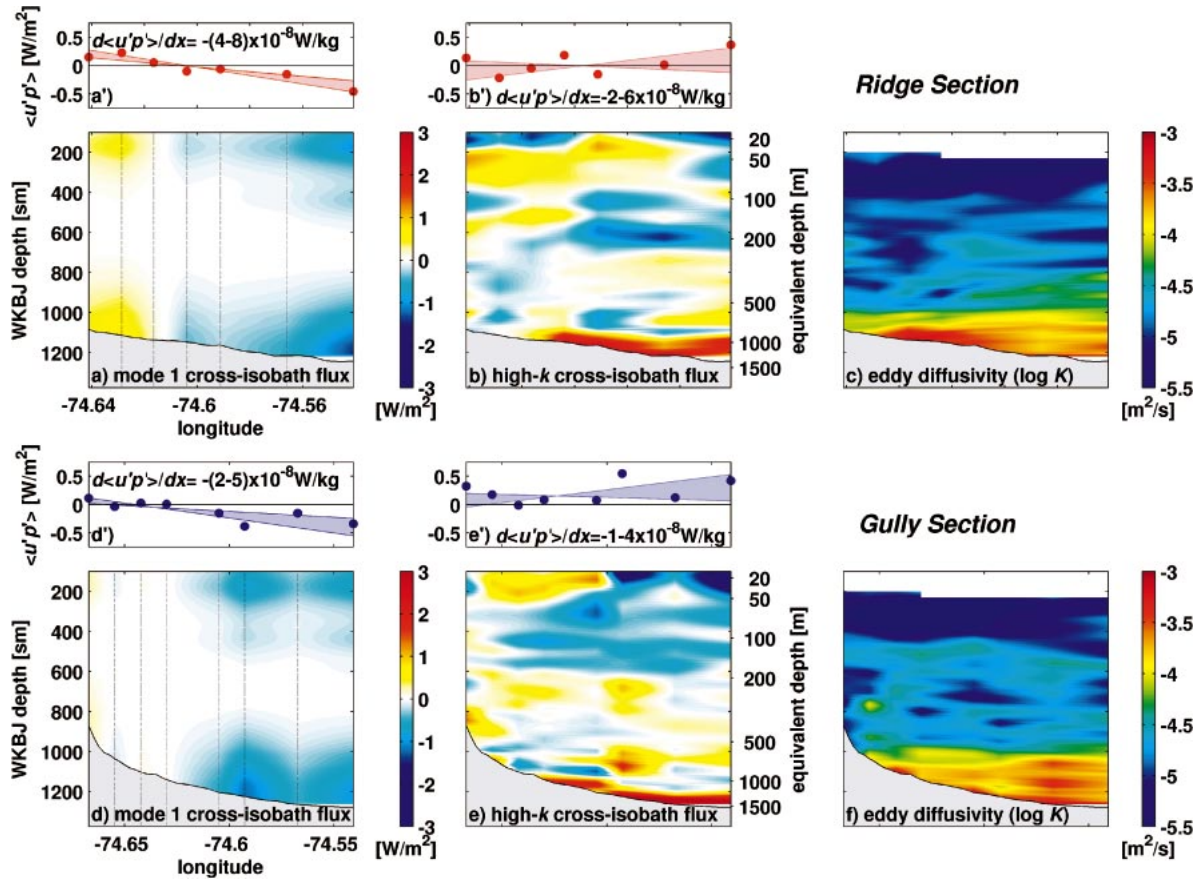


FIG. 12. Spatial distribution of cross-isobath energy flux  $\langle u'p' \rangle$  and inferred eddy diffusivity  $K_p$  along a ridge top (top row) and through its neighboring gully (bottom row): (a), (d) energy flux computed from projections onto the mode-1 structure functions for  $u'$  and  $p'$ ; (b), (e) high wavenumbers (total flux minus mode 1). Vertically averaged energy-flux and bootstrap linear fits are shown above each plot [(a'), (b'), (d'), (e')]; shading represents 90% confidence limits on the slope, as bootstrapped from 1000 linear regression estimates of a randomly sampled data with replacement. Depth averages of mode 1 (a', d') are computed over the full water column. The upper 150 m were omitted in the high-wavenumber vertical averages [(b'), (c')] because these may be influenced by fluxes from waves of near-surface origin. The eddy diffusivity inferred from the Gregg–Henyey scaling applied to the finescale shear [(c'), (f')] is intensified near the bottom below 1000 m, approaching  $10 \times 10^{-4} \text{ m}^2 \text{ s}^{-1}$ . The low-mode convergence, near-bottom beam and distribution of  $K_p$  have similar character along a ridge top (top row) and its neighboring gully (bottom row). Note that the longitudinal extents of the ridge and gully plots differ.

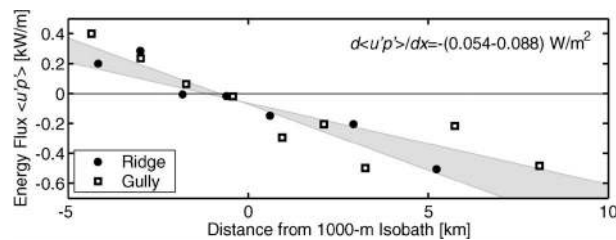


FIG. 13. Full-depth integrals of the cross-isobath energy flux (all modes) are plotted as a function of the distance from the 1000-m isobath to collapse ridge and gully sections and enable the net cross-isobath energy-flux convergence to be computed using all data. The shading represents 90% bootstrap confidence limits on the slope (see Fig. 12). The depth-integrated convergence indicated in the figure corresponds to  $(-7 \pm 2) \times 10^{-8} \text{ W kg}^{-1}$  at the 1000-m isobath.

inated by semidiurnal frequencies within 250 m of the bottom (Fig. 9).

- 2) Intensified near-bottom shear appears to be bounded above by a semidiurnal internal wave characteristic emerging below the 900-m isobath (Fig. 5).
- 3) Vertically homogenized BBLs are only observed offshore of the 800-m isobath (Fig. 4) and are much thinner than the intensified stratified shear.
- 4) Cross-isobath energy-flux convergence in the low modes roughly balances the high-wavenumber divergence below 150-m depth, with a residual of  $(2 \pm 5) \times 10^{-8} \text{ W kg}^{-1}$ . The average turbulent energy dissipation rate near the bottom is  $\sim 0.5 \times 10^{-8} \text{ W kg}^{-1}$ . In addition, the baroclinic energy density is increasing at a rate of  $\sim 1 \times 10^{-8} \text{ W kg}^{-1}$ .

These indicate that the intensified shear, dissipation, and diffusivity could result from the response of a low-mode semidiurnal tide to the large-scale shape of the continental slope.



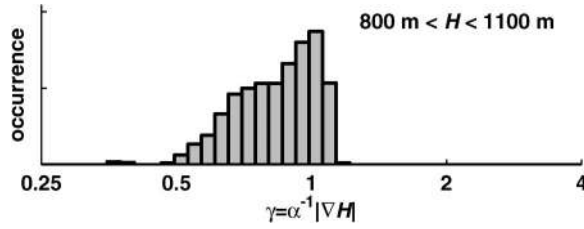


FIG. 14. Distribution of bottom slopes  $s/\alpha$  between  $36.5^\circ$  and  $36.75^\circ\text{N}$  and between the 800- and 1100-m isobaths, as computed from high-resolution bathymetry smoothed to 10-km resolution; 78% of bottom slopes are within 30% of critical.

To aid this interpretation, we address a number of questions in the following sections.

Section 3a: In linear theory, can reflection of a mode-1 internal tide propagating onto the Virginia continental slope give rise to the observed high-wavenumber response, shear intensification, and unstable Ri numbers?

Section 3b: Can planar reflection theory applied to realistic 2D topography explain the observed energy flux distribution? Is the northward along-isobath energy flux consistent with this hypothesis?

Section 3c: Could reflection/scattering of the internal tide from the corrugations be an alternative mechanism for generating unstable shear?

Section 3d: Where is the source of the incident internal tide and why does it vary so dramatically in time?

#### a. Reflection from an inclined plane

Following Eriksen (1982, 1985), we consider reflection of an internal wave from a sloping bottom ( $z = -sx$ ). The ratio of reflected to incident wavenumbers  $[k_z^{(r)}/k_z^{(i)}]$  and amplitudes  $[u^{(r)}/u^{(i)}]$  is given by the reflection ratio,

$$R = \frac{k_z^{(r)}}{k_z^{(i)}} = \frac{u^{(r)}}{u^{(i)}} = -\frac{(1 \pm s/\alpha)}{(1 \mp s/\alpha)}, \quad (9)$$

where  $\alpha = \pm\sqrt{(\omega^2 - f^2)/(N^2 - \omega^2)}$  for an internal wave of frequency  $\omega$ . The ratio  $R$  is unity only for limiting cases ( $s = 0$ ,  $s = \infty$ ,  $\alpha = 0$ , or  $\alpha = \infty$ ). Linear theory predicts amplification when the slope of internal wave characteristics is similar to the bottom slope ( $\alpha \sim s$ ). At  $\alpha = s$ ,  $R = -\infty$ . The case of large  $|R|$  is of particular interest here, as it leads to high shear and increased likelihood of turbulence.

If a mode-1 internal tide ( $\lambda_z = 2H = 3000$  m;  $H$  is the water depth) reflects to produce waves with  $\lambda_z = 300$  m (as observed) then  $[k_z^{(r)}/k_z^{(i)}] = 10$ , which requires  $s/\alpha = 0.8$  or  $s/\alpha = 1.2$  (9). The distribution of bottom slopes along the Virginia continental slope (Fig. 14) indicates that both of these values of the bottom slope are common near and onshore of the 1100-m isobath.

The squared vertical shear  $S^2 = (du/dz)^2 + (dv/dz)^2$  in the reflected wave field is related to that of the incident field by

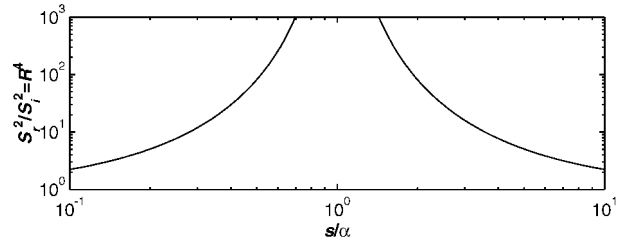


FIG. 15. Ratio of squared shear for the reflected wave to that of the incident wave as a function of slope ratio  $s/\alpha$ .

$$S_r^2 = R^4 S_i^2, \quad (10)$$

as shown in Fig. 15. For  $\alpha$  within 30% of  $s$ ,  $S_r^2/S_i^2 > 1000$ . If wave breakdown occurs through wave-wave interactions of the type envisioned by Henyey et al. (1986), then one would expect turbulent dissipation to scale with  $S^4$ . Hence, a more than  $10^6$ -fold increase in dissipation would be associated with a wave field reflected from a moderately near-critical slope ( $0.7 < s/\alpha < 1.3$ ). Such slope ratios comprise 32% of the bottom slopes between the 500- and 1500-m isobaths on the Virginia slope and 78% of those between the 800- and 1100-m isobaths (Fig. 14).

Interactions with nearly critical slope  $s$  could also directly lead to mixing through shear instability associated with  $\text{Ri} < 1/4$ . These may act locally to break down the most unstable waves, yet permit stable waves to propagate into the interior to later produce turbulence through the mechanism suggested by Gregg-Henyey (Gregg 1989). For example, consider the shoaling of a mode-1 internal tide with a  $2 \text{ cm s}^{-1}$  WKB amplitude ( $0.4 \text{ kW m}^{-1}$ , consistent with Fig. 13). Near the 1000-m isobath, the mean squared shear associated with such a first-mode wave is  $S^2 \sim 10^{-10} \text{ s}^{-2}$ . Given a bottom stratification  $N^2 \sim 10^{-6} \text{ s}^{-2}$ , a  $(10^4\text{--}10^5)$ -fold increase in  $S^2$  would produce unstable  $\text{Ri} \sim 1/4$ . Bottom slopes within 20% of critical could produce this intensification.

#### b. A ray-tracing approach

To better demonstrate that wave reflection may lead to the observed energy-flux distribution, a ray-tracing model (9) of the wave-topography interaction is used. We assume 2D bathymetry, neglecting alongshore topographic variability. Computations were performed over a 100-km cross-isobath and 1500-sm-deep constant stratification domain. To focus on the deep dynamics (i.e., near 1000 sm), we neglect the continental shelf by extending the continental slope to the surface at the shelf break. The incident wave field is a sum of rays comprising a mode-1 vertically standing wave at the offshore boundary ( $x = 100$  km) with zonal velocity amplitudes chosen to produce a shoreward energy flux of  $0.4 \text{ kW m}^{-1}$ . Information about the wave amplitude is assumed to be transmitted along characteristics until they leave the domain. Surface reflections alter only the vertical propagation direction  $[k_z^{(r)} = -k_z^{(i)}]$ . Topographic

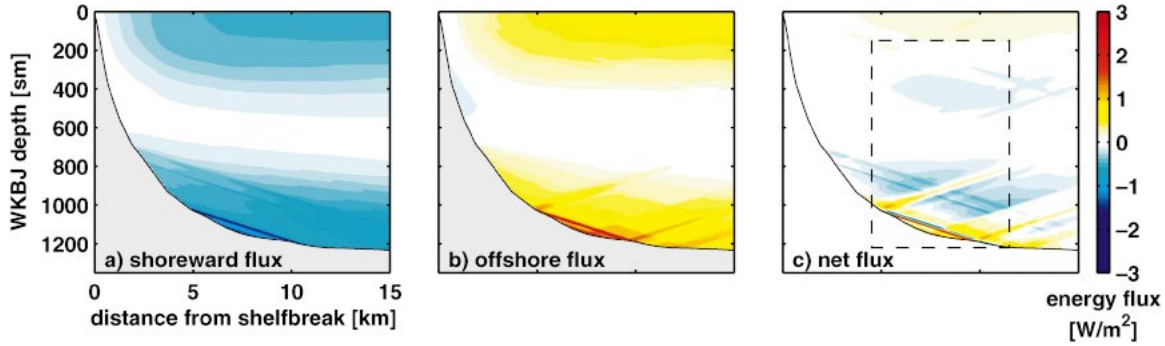


FIG. 16. Energy flux associated with the reflection of a  $0.4 \text{ kW m}^{-1}$  mode-1 internal tide from the Virginia slope. The (a) incident and (b) reflected energy fluxes are mode 1 plus higher-wavenumber intensification near the bottom. (c) The net energy flux is dominated by the high-wavenumber motions, as the incident and reflected low-mode contributions are approximately equal. The high- $k$  energy flux has both on- and offshore components of magnitudes  $\sim 4 \text{ W m}^{-2}$ , several times that of the incident mode-1 energy flux ( $\sim 1 \text{ W m}^{-2}$ ). The area in the dashed box corresponds to that in Figs. 12a–c.

reflections follow (9) after Eriksen (1982). Subcritical bottom reflection alters vertical propagation direction and amplitude [ $k_z^{(r)} = -Rk_z^{(i)}$ ,  $k_x^{(r)} = Rk_x^{(i)}$ ,  $u^{(r)} = Ru^{(i)}$ ]. Supercritical reflection alters horizontal propagation direction and amplitude [ $k_z^{(r)} = Rk_z^{(i)}$ ,  $k_x^{(r)} = -Rk_x^{(i)}$ ,  $u^{(r)} = -Ru^{(i)}$ ]. Vertical displacements were computed by integrating vertical velocity in time; pressure anomalies were computed using (1).

Figure 16 shows the time-averaged energy flux in the shoreward, seaward, and net fields. The shore- and seaward fields are intensified near critical slopes, dramatically increasing amplitudes and wavenumbers. As a result, high-wavenumber fluxes propagating both on- and offshore are produced (Fig. 16c). In the absence of dissipation, these form beams that propagate until they leave the domain. In reality, these beams would be unstable and dissipate by turbulence. Destructive interference between on- and offshore beams would therefore be reduced (Gilbert and Garrett 1989; Legg and Adcroft 2003).

Concave continental slopes are often overlooked for their potential for strong internal-wave-topography interactions because analytic solutions (Gilbert and Garrett 1989) and observations (Gilbert 1993; Zervakis et al. 2003) suggest that they are much less efficient at intensifying shear than convex ones. However, Gilbert and Garrett's (1989) results were based on a single analytic form (parabolic) for the bottom slope. While this particular choice allowed for an exact analytic solution, it also has a unique property that the amplitudes of upslope and downslope (incident and reflected) wavefields were equal, resulting in destructive interference. From our ray-tracing solutions, only these parabolic slopes produce complete destructive interference, while more-realistic concave slopes produce complex high-wavenumber interference patterns. Recent numerical simulations in which this symmetry is not required (Legg and Adcroft 2003) find a similar intensification of high wavenumbers over both concave and convex slopes. Observations have also provided anecdotal ev-

idence that enhanced dissipation can occur over concave slopes (Toole et al. 1997). This has important implications, because most continental slopes are concave in a WKB-stretched sense. They should not be overlooked as potential sites of mixing.

Despite the many simplifying assumptions, we find a qualitative similarity of the wavenumber content and high- $k$  energy flux in comparing Figs. 16c and 12b,e. This confirms that the idealized mechanics hypothesized in section 3a are plausible.

#### HORIZONTALLY STANDING MODES

Since our calculations are inviscid, no net energy-flux convergence is possible, and the vertically integrated energy flux of the reflected field is approximately equal and opposite to the incident. This forms a horizontally standing mode with weak net cross-isobath energy flux (Fig. 16c). A peculiar feature of the standing wave is that the along-slope flux  $\langle v'p' \rangle$  does not vanish, but instead has a significant northward component ( $0.5 \text{ kW m}^{-1}$  within 20 km of the coast).

This artifact can be illustrated by considering the energy flux associated with a superposition of two first-mode waves, one propagating in the  $-x$  direction (the incident wave) and the other in the  $+x$  direction (the reflected wave) having vertical and zonal wavenumbers of  $k_z^o = \pi/H$  and  $k_x^o = \alpha k_z^o \sim 2\pi/(80 \text{ km})$ . Each wave carries a zonal energy flux of  $\pm \frac{1}{2} u_o p_o \cos^2(k_z^o z)$ , where  $u_o$  and  $p_o$  are the modal amplitudes of zonal velocity and pressure. They are phased to produce no normal flow across a vertical wall at  $x = 0$ . While the cross-isobath energy flux  $\langle u'p' \rangle$  of the combined wavefield is zero everywhere, the correlation between pressure anomaly of the incident (reflected) wave and the transverse velocity of the reflected (incident) wave is nonzero and produces an alongshore energy flux:

$$v'p' = \left( \frac{u_o p_o f}{\omega} \right) \sin(2k_x^o x) \cos^2(k_z^o z), \quad (11)$$

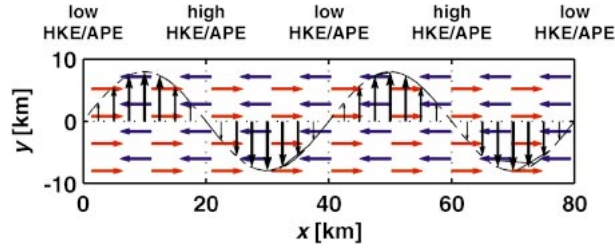


FIG. 17. Hypothetical variability in internal wave energy flux for a standing wave formed when a westward-propagating wave (blue arrows) with  $\lambda_x = 80$  km reflects from a north-south wall at  $x = 0$  (red arrows). While the total zonal flux is zero at all locations, the along-slope flux (black arrows) has bands of positive and negative  $\langle v'p' \rangle$  at quarter-wavelength intervals. To adequately represent the energy flux,  $\mathbf{u}'p'$  must be averaged over at least one-half wavelength. Regions of enhanced HKE/APE are indicated.

as illustrated by Fig. 17. Maxima  $\langle v'p' \rangle_{\text{total}}$  occur at  $x = (2n - 1)\pi/(4k_x^o)$  and have a magnitude that locally exceeds the spatially uniform energy flux in either the incident or reflected propagating waves. This explains the observed along-slope energy fluxes (Fig. 11). A signature of such a superposition is that the strongest baroclinic velocities are not aligned in the direction of the net energy flux as we observe (Fig. 10).

In addition, time- and depth-averaged energy densities of a horizontally standing mode have offshore structure:

$$\text{APE} = \frac{u_o^2 N^2 \alpha^2}{2\omega^2} \cos^2(k_x^o x), \quad (12)$$

$$\text{HKE} = \frac{1}{2} u_o^2 \sin^2(k_x^o x) \left( 1 + \frac{f^2}{\omega^2} \right). \quad (13)$$

As compared with a single propagating wave for which  $\text{HKE}/\text{APE} = (\omega^2 + f^2)/(\omega^2 - f^2)$  uniformly, the ratio  $\text{HKE}/\text{APE}$  for a horizontally standing mode varies periodically. It is 0 at  $x = n\pi\lambda_x/2$  and  $\infty$  at  $x = (2n + 1)\lambda_x/4$  for  $n = 0, 1, 2, 3, \dots$ . Hence, a signature of a standing mode is decreased  $\text{HKE}/\text{APE}$  near the boundary, as observed during the later period of strong internal wave activity (Fig. 10), and enhanced  $\text{HKE}/\text{APE}$  one-quarter wavelength offshore.

#### c. Interactions with corrugations

Scattering of the low-mode  $M_2$  internal tide off the cross-isobath corrugations is another possible mechanism for generating finescale internal waves that would break and produce elevated turbulence. From Thorpe (2001), one would expect the along-slope wavenumber of the reflected wave field to match that of the local bathymetry (having along-slope wavevector  $k_{\text{bathy}}$ ). To conserve frequency, this requires

$$\frac{k_z^{(r)}}{\sqrt{[k_x^{(r)}]^2 + k_{\text{bathy}}^2}} = \frac{k_z^{(i)}}{\sqrt{[k_x^{(i)}]^2 + [k_y^{(i)}]^2}} = \alpha^{-1}, \quad (14)$$

where  $\alpha^{-1} \approx 30$ ,  $[k_x^{(i)}, k_y^{(i)}, k_z^{(i)}]$  and  $[k_x^{(r)}, k_y^{(r)}, k_z^{(r)}]$  are the wavevectors of the incident and reflected fields, and  $k_y^{(r)} = k_{\text{bathy}} = 2\pi/\lambda_{\text{bathy}} = 2 \text{ km}^{-1}$ . Assuming  $k_x^{(r)} = 0$  allows calculation of the lowest vertical wavenumber  $k_z^{(r)}$  (the largest wavelength) associated with  $M_2$  interaction with the corrugations. This yields

$$k_z^{(r)} > \alpha^{-1} k_{\text{bathy}} \approx 0.06 \text{ m}^{-1}, \quad (15)$$

which corresponds to vertical wavelengths of 100 m and smaller. This contrasts with the 300-m vertical wavelengths that we observe to dominate the near-bottom signal. Hence, scattering off the corrugations does not appear to be responsible for the observed shears. This is further supported by our observations that neither the variability in the high- $k$  internal wave field nor the dissipation rate was clearly tied to the corrugation length scale. However, high-wavenumber scattering from the corrugations (15) may dissipate rapidly enough that a layer of enhanced turbulence is produced without developing a phase-locked internal wave field. Our data cannot rule out this possibility.

#### d. Source and variability of the internal tide

Until this point, we have not specified a source for the incident, low-mode baroclinic tide nor discussed reasons for its temporal variability. In this section, we explore some possibilities.

A possible source for the internal tide is the local shelf break. However, numerical simulations performed by Legg (2004a) suggest that the vertically integrated energy flux from the shelf break is weak ( $<0.05 \text{ kW W m}^{-1}$ ) for typical barotropic cross-isobath forcing. This is in contrast to regions like the Bay of Biscay (Pingree and New 1991) where the cross-isobath barotropic forcing is strong and the internal tide forms at the shelf break. The Virginia shelf break is more typical of continental margins for which the barotropic forcing across the shelf break is weak (Baines 1982; Sjöberg and Stigebrandt 1992).

More important is that baroclinic motions from a shelf-break-generated tide do not penetrate below the downward semidiurnal characteristic originating at the shelf break. This contrasts our observations of strong semidiurnal shear in the lower water column. Legg (2004b) also performed simulations with along-slope barotropic forcing and concluded that bottom-intensified shear was generated by the corrugations, but was only of small amplitude for reasonable barotropic forcing.

As the locally generated internal tide seems incapable of generating the observed deep shears, we search for a remote source by exploring some deep-ocean data. Unfortunately, baroclinic velocity data were not collected offshore of the Virginia slope during this experiment. However, a 2-yr record of velocity and temperature at  $34^\circ\text{N}$ ,  $70^\circ\text{W}$  was collected during the Long Term Upper Ocean Study (LOTUS; Tarbell et al. 1985) and is used to assess the strength of the deep-ocean internal



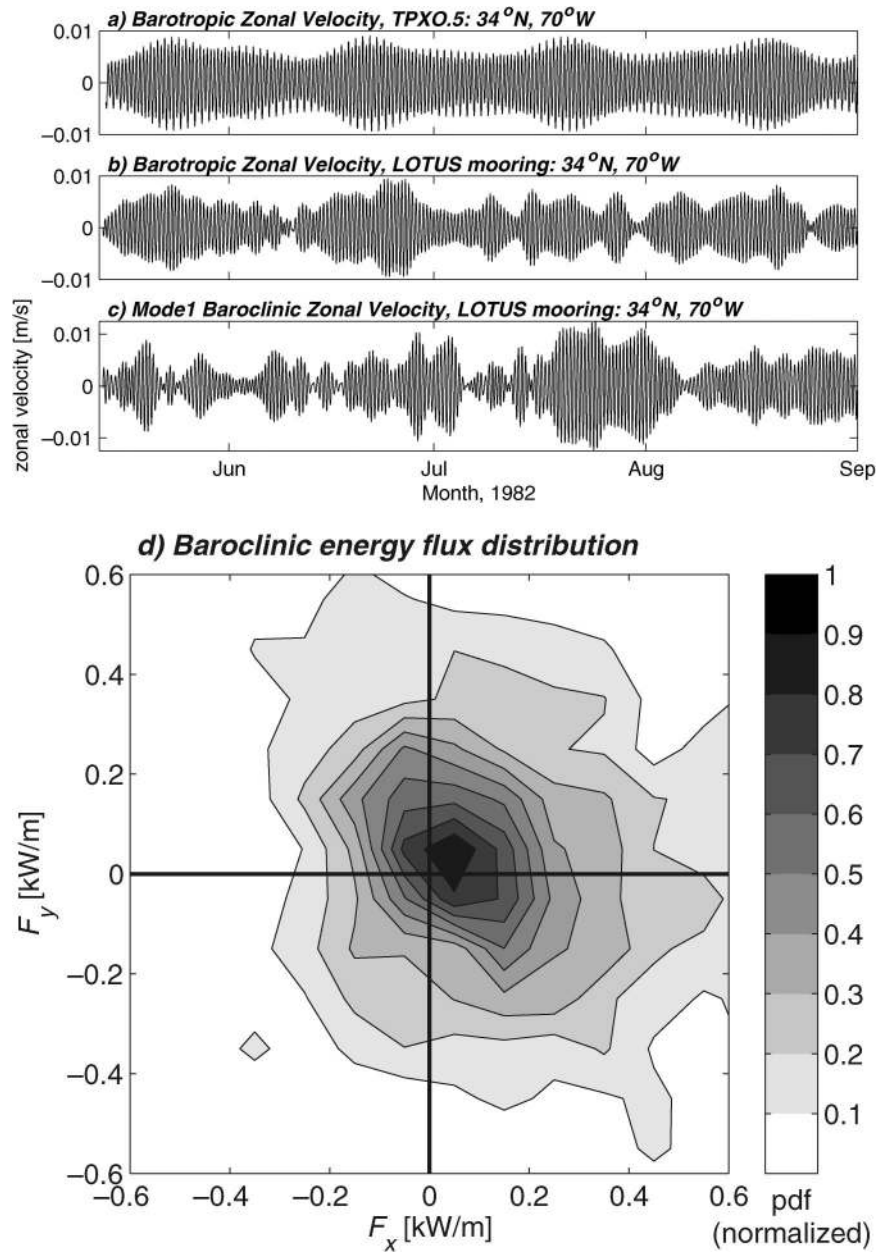


FIG. 18. Strength and temporal variability of the semidiurnal tide at 34°N, 70°W, 500 km SE of the TWIST site, May–Sep 1982. Zonal velocity component of the barotropic tide as predicted by (a) TPX0.5 (Egbert 1997) and (b) as estimated from mode fits to 12 current meters spanning 100–4000 m on the LOTUS mooring in 1982 (Tarbell et al. 1985; data bandpassed at  $12.4 \pm 2$  h). (c) Measured amplitude of the first baroclinic mode of zonal velocity at the LOTUS site. (d) Distribution of the depth-integrated energy flux (zonal  $F_x$ , meridional  $F_y$ ) in the first three modes using 450 days of data between May 1982 and Oct 1983.

tide and its variability. The measured barotropic velocity (Fig. 18b) exhibits more temporal variability than the TPX0.5 barotropic tide prediction (Fig. 18a). The estimated mode-1 baroclinic tide (Fig. 18c) is even more variable in time with its amplitude only loosely linked to the barotropic spring–neap cycle.

The median and mean vertically integrated energy

fluxes over the 450-day period are 0.35 and 0.5  $\text{kW m}^{-1}$ , respectively; estimates exceeding 1  $\text{kW m}^{-1}$  occur 6% of the time. On average, the depth-integrated energy flux is directed northeast [away from the Blake Escarpment—a possible generation site; Hendry (1977)] with 18% of the estimates directed northwest (toward the Virginia slope) with an average magnitude of 0.35  $\text{kW}$

$\text{m}^{-1}$ . We hypothesize that these internal tides could survive multiple surface/bottom reflections, as their more energetic counterparts do in the Pacific Ocean (Ray and Mitchum 1996; Cummins et al. 2001). Since northward-propagating internal tides encountering zonal bathymetric slopes will gradually refract shoreward and eventually propagate fully upslope (Thorpe 2001; Fig. 2), even the northeastward-propagating internal tides at LOTUS may shoal on the Virginia slope. We conclude that deep-ocean internal tides in the North Atlantic are sufficiently energetic to be a possible source for the observed energy fluxes at the Virginia slope.

Several factors may explain the abrupt appearance of the semidiurnal tide after 29 May in our observations. In addition to the fortnightly spring–neap cycle, the internal tide is modulated on subinertial time scales through interaction with temporally variable stratification and Doppler-shifting by geostrophic currents. Both of these can alter propagation over long distances and produce highly intermittent internal tides (Wunsch 1975). Currents from the nearby meandering Gulf Stream system ( $\sim 1 \text{ m s}^{-1}$ , comparable to the mode-1 phase speed) could also significantly modulate internal tides by deflecting their ray paths. Local along-isobath currents are likely to have only a minor effect as they could account for a frequency shift  $\Delta\omega = k_y v = 9 \times 10^{-6} \text{ rad s}^{-1}$  of only 10% of  $M_2$  (assuming a mode-1 horizontal wavenumber  $k_y \sim 9 \times 10^{-5} \text{ rad m}^{-1}$  and along-isobath current  $v \sim 0.1 \text{ m s}^{-1}$ ).

#### 4. Conclusions

Elevated turbulence dissipation ( $\epsilon \sim 10^{-8} \text{ W kg}^{-1}$ ) and mixing ( $K_p \sim 10^{-3} \text{ m}^2 \text{ s}^{-1}$ ) was observed over the Virginia continental slope. A likely source for this turbulence is reflection and scattering of a remotely generated internal tide incident on the near-critical slope, producing a high vertical-wavenumber response. The associated finescale shears have intensity sufficient to support unstable  $Ri$ .

Estimates of the cross-isobath semidiurnal energy flux  $\langle u'p' \rangle$  indicate that low modes are propagating onshore and converging, whereas high wavenumbers are generated and propagate offshore. A high-wavenumber beam is observed to originate near the 900-m isobath (Figs. 12b,e) and coincides with the layer of elevated diffusivity (Figs. 12b,e). The net cross-isobath energy-flux convergence of  $d\langle u'p' \rangle/dx = (7 \pm 2) \times 10^{-8} \text{ W kg}^{-1}$  is partially balanced by an along-isobath flux divergence  $d\langle v'p' \rangle/dy = (3 \pm 2) \times 10^{-8} \text{ W kg}^{-1}$  to yield a net baroclinic flux convergence  $[\nabla \cdot \langle \mathbf{u}'p' \rangle] = (4 \pm 4) \times 10^{-8} \text{ W kg}^{-1}$ . While  $\sim 1 \times 10^{-8} \text{ W kg}^{-1}$  is required to increase the baroclinic energy density over the slope, the remainder must be lost to turbulent dissipation and mixing or be radiated as incoherent high modes that are unresolved by this analysis. Based on the observed dissipation rates and energy-flux estimates, the high modes should be able to propagate  $\sim 100 \text{ km}$  before dissipating,

providing a mechanism for communicating energy for turbulent mixing into the ocean interior.

Energy fluxes of  $0.3\text{--}1 \text{ kW m}^{-1}$  are typical of semidiurnal internal tides throughout the world's oceans (Alford 2003). Since most continental slopes are somewhere supercritical with respect to the semidiurnal tide, they must also have regions of near-critical slopes, which may cause reflection/scattering of the internal tide in a manner similar to that on the Virginia slope. For example, elevated dissipation rates were observed by Moun et al. (2002) over a near-critical section of the Oregon continental slope. A reanalysis of the Slope Undercurrent Study dataset (Huyer et al. 1984) for internal tides indicates that  $0.5 \text{ kW m}^{-1}$  onshore energy fluxes are not uncommon and that there is a net low-mode energy flux convergence onto the slope. This suggests that internal wave reflection may produce enhanced mixing on the Oregon slope. Regions of well-mixed fluid may then form and spread buoyantly into the ocean interior to form intermediate nepheloid layers (McPhee-Shaw and Kunze 2002). Such intrusions may transport fluid along isopycnals many kilometers from their source and be identified by the unique  $T$ ,  $S$ , potential vorticity, and suspended sediment loading associated with the region where they detached from the bottom (Armi 1978; Kunze and Sanford 1993; Moun et al. 2002).

If the Virginia slope is typical of continental slopes around the world, then regions of elevated turbulent dissipation and mixing may be identified from bathymetric maps and a knowledge of the internal wave field. Smoothed seafloor topography, such as Smith and Sandwell (1997), may be useful for identifying regions of near-critical bottom topography, and global fields of internal tide energy flux may be estimated using existing mooring data (Alford 2003), although this coverage is sparse. Combining these with generalized results from nonlinear wave breaking models (Legg and Adcroft 2003) may permit determination of low-mode internal tide dissipation and quantification of its role in global mixing budgets.

*Acknowledgments.* The captain and crew of the R/V *Oceanus* are to be commended for their efforts. Art Bartlett, Dicky Allison, Karin Gustafsson, and Luca Centurioni are thanked for their help at sea. Shipboard ADCP sampling used to reference the XCP velocity profiles was made available by Ellyn Montgomery. Kurt Polzin provided the HRP data and many insights. Thanks are given also to Dave Wellwood, Steve Liberatore, and John Kemp for their help with HRP and MP deployments, and to Lou St. Laurent and an anonymous reviewer for their helpful comments on this manuscript. This research was funded by the Office of Naval Research under Grants N00014-94-10038 and N00014-97-10087.

## REFERENCES

- Alford, M. H., 2003: Energy available for ocean mixing redistributed by long-range propagation of internal waves. *Nature*, **423**, 159–162.
- Althaus, A. M., E. Kunze, and T. B. Sanford, 2003: Internal tide radiation from Mendicino Escarpment. *J. Phys. Oceanogr.*, **33**, 1510–1527.
- Armi, L., 1978: Some evidence for boundary mixing in the deep ocean. *J. Geophys. Res.*, **83**, 1971–1979.
- Baines, P. G., 1982: On internal tide generation models. *Deep-Sea Res.*, **29**, 307–338.
- Balmforth, N., G. Ierley, and W. Young, 2002: Tidal conversion by subcritical topography. *J. Phys. Oceanogr.*, **32**, 2900–2914.
- Bell, T. H., 1975: Topographically generated internal waves in the open ocean. *J. Geophys. Res.*, **80**, 320–327.
- Cacchione, D. A., L. F. Pratson, and A. S. Ogston, 2002: The shaping of continental slopes by internal tide. *Science*, **296**, 724–727.
- Carter, G. S., and M. C. Gregg, 2002: Intense variable mixing near the head of Monterey Submarine Canyon. *J. Phys. Oceanogr.*, **32**, 3145–3165.
- Cummins, P. F., J. Y. Cherniawski, and M. G. Foreman, 2001: North Pacific internal tides from the Aleutian Ridge: Altimeter observations and modelling. *J. Mar. Res.*, **59**, 167–191.
- Doherty, K. W., D. E. Frye, S. P. Liberatore, and J. M. Toole, 1999: A moored profiling instrument. *J. Atmos. Oceanic Technol.*, **16**, 1816–1829.
- Egbert, G. D., 1997: Tidal data inversion: Interpolation and inference. *Progress in Oceanography*, Vol. 40, Pergamon, 81–108.
- Eriksen, C. C., 1982: Observations of internal wave reflection off sloping bottoms. *J. Geophys. Res.*, **87** (C1), 525–538.
- , 1985: Implication of ocean bottom reflection for internal wave spectra and mixing. *J. Phys. Oceanogr.*, **15**, 1145–1156.
- , 1998: Internal wave reflection and mixing at Fieberling Guyot. *J. Geophys. Res.*, **103**, 2977–2994.
- Ferron, B., H. Mercier, K. Speer, A. Gargett, and K. Polzin, 1998: Mixing in the Romanche Fracture Zone. *J. Phys. Oceanogr.*, **28**, 1929–1945.
- Gerkema, T., 2001: Internal and interfacial tides: Beam scattering and local generation of solitary waves. *J. Mar. Res.*, **59**, 227–255.
- , 2002: Application of an internal tide generation model to baroclinic spring–neap cycles. *J. Geophys. Res.*, **107**, 3124, doi:10.1029/2001JC001177.
- Gilbert, D., 1993: A search for evidence of critical internal wave reflection on the continental rise and slope off Nova Scotia. *Atmos.–Ocean*, **31**, 99–122.
- , and C. Garrett, 1989: Implications for ocean mixing of internal wave scattering off irregular topography. *J. Phys. Oceanogr.*, **19**, 1716–1729.
- Gregg, M. C., 1989: Scaling turbulent dissipation in the thermocline. *J. Geophys. Res.*, **94** (C5), 9686–9698.
- Hendry, R. M., 1977: Observations of the semidiurnal internal tide in the western North Atlantic Ocean. *Philos. Trans. Roy. Soc. London*, **286A**, 1–24.
- Heney, F. S., J. Wright, and S. M. Flatte, 1986: Energy and action flow through the internal wave field: An eikonal approach. *J. Geophys. Res.*, **91**, 8487–8495.
- Huyer, A., R. L. Smith, and B. M. Hickey, 1984: Observations of a warm-core eddy off Oregon, January to March 1978. *Deep-Sea Res.*, **31**, 97–117.
- Jayne, S. R., and L. C. St. Laurent, 2001: Parameterizing tidal dissipation over rough topography. *Geophys. Res. Lett.*, **28**, 811–814.
- Klymak, J. M., and M. C. Gregg, 2004: Tidally generated turbulence over the Knight Inlet sill. *J. Phys. Oceanogr.*, **34**, 1135–1151.
- , J. N. Moum, and A. Perlin, 2002: Observations of boundary mixing in the Hawaiian ridge system. *Eos, Trans. Amer. Geophys. Union Ocean Sciences Meet. Suppl.*, **83**, Abstract OS41E-77.
- Kunze, E., and T. B. Sanford, 1993: Submesoscale dynamics near a seamount. Part I: Measurements of Ertel vorticity. *J. Phys. Oceanogr.*, **23**, 2567–2588.
- , and J. M. Toole, 1997: Tidally driven vorticity, diurnal shear, and turbulence atop Fieberling seamount. *J. Phys. Oceanogr.*, **27**, 2663–2693.
- , L. K. Rosenfeld, G. S. Carter, and M. C. Gregg, 2002a: Internal waves in Monterey Submarine Canyon. *J. Phys. Oceanogr.*, **32**, 1890–1913.
- , T. B. Sanford, C. M. Lee, and J. D. Nash, 2002b: Internal tide radiation and turbulence along the Hawaiian Ridge. *Eos, Trans. Amer. Geophys. Union Ocean Sciences Meet. Suppl.*, **83**, Abstract OS32P-01.
- Legg, S., 2004a: Internal tides generated on a corrugated continental slope. Part I: Cross-slope barotropic forcing. *J. Phys. Oceanogr.*, **34**, 156–173.
- , 2004b: Internal tides generated on a corrugated continental slope. Part II: Along-slope barotropic forcing. *J. Phys. Oceanogr.*, in press.
- , and A. Adcroft, 2003: Internal wave breaking at concave and convex continental slopes. *J. Phys. Oceanogr.*, **33**, 2224–2246.
- Lien, R., and M. Gregg, 2001: Observations of turbulence in a tidal beam and across a coastal ridge. *J. Geophys. Res.*, **106**, 4575–4592.
- Lueck, R. G., and T. D. Mudge, 1997: Topographically induced mixing around a shallow seamount. *Science*, **276**, 1831–1833.
- MacCready, P., and G. Pawlak, 2001: Stratified flow along a rough slope: Separation drag and wave drag. *J. Phys. Oceanogr.*, **31**, 2824–2839.
- McPhee-Shaw, E. E., and E. Kunze, 2002: Boundary-layer intrusions from a sloping bottom: A mechanism for generating intermediate nepheloid layers. *J. Geophys. Res.*, **107**, 3050, doi:10.1029/2001JC000801.
- Merrifield, M. A., and P. E. Holloway, 2002: Model estimates of  $m_2$  internal tide energetics at the Hawaiian Ridge. *J. Geophys. Res.*, **107**, 3179, doi:10.1029/2001JC000996.
- , —, and T. M. S. Johnston, 2001: Internal tide generation at the Hawaiian Ridge. *Geophys. Res. Lett.*, **28**, 559–562.
- Moum, J. N., D. Caldwell, J. D. Nash, and G. Gundersen, 2002: Observations of boundary mixing over the continental slope. *J. Phys. Oceanogr.*, **32**, 2113–2130.
- Müller, P., and N. Xu, 1992: Scattering of oceanic internal gravity waves off random bottom topography. *J. Phys. Oceanogr.*, **22**, 474–488.
- , and X. Liu, 2000a: Scattering of internal waves at finite topography in two dimensions. Part I: Theory and case studies. *J. Phys. Oceanogr.*, **30**, 532–549.
- , and —, 2000b: Scattering of internal waves at finite topography in two dimensions. Part II: Spectral calculations and boundary mixing. *J. Phys. Oceanogr.*, **30**, 550–563.
- Munk, W., 1981: Internal waves and small-scale processes. *Evolution of Physical Oceanography: Scientific Surveys in Honor of Henry Stommel*, B. A. Warren and C. Wunsch, Eds., The MIT Press, 264–291.
- , and C. Wunsch, 1998: Abyssal recipes II: Energetics of tidal and wind mixing. *Deep-Sea Res.*, **45**, 1977–2010.
- Nash, J. D., and J. N. Moum, 2001: Internal hydraulic flows on the continental shelf: High drag states over a small bank. *J. Geophys. Res.*, **106** (C3), 4593–4611.
- Osborn, T. R., 1980: Estimates of the local rate of vertical diffusion from dissipation measurements. *J. Phys. Oceanogr.*, **10**, 83–89.
- Pingree, R. D., and A. L. New, 1989: Downward propagation of internal tidal energy into the Bay of Biscay. *Deep-Sea Res.*, **36**, 735–758.
- , and —, 1991: Abyssal penetration and bottom reflection of internal tide energy into the Bay of Biscay. *J. Phys. Oceanogr.*, **21**, 28–39.
- Polzin, K. L., 2004: Idealized solutions for the energy balance of the finescale internal wave field. *J. Phys. Oceanogr.*, **34**, 231–246.
- , K. Speer, J. M. Toole, and R. W. Schmitt, 1996: Intense mixing



- of Antarctic Bottom Water in the equatorial Atlantic. *Nature*, **380**, 54–57.
- Prinsenbergh, S. J., W. L. Wilmot, and M. Rattray Jr., 1974: Generation and dissipation of coastal internal tides. *Deep-Sea Res.*, **21**, 263–281.
- Ray, R. D., and G. T. Mitchum, 1996: Surface manifestation of internal tides generated near Hawaii. *Geophys. Res. Lett.*, **23**, 2101–2104.
- Rudnick, D. L., and Coauthors, 2003: From tides to mixing along the Hawaiian Ridge. *Science*, **301**, 355–357.
- Sanford, T. B., E. A. D'Asaro, E. L. Kunze, J. H. Dunlap, R. G. Drever, M. A. Kennelly, M. D. Prater, and M. S. Horgan, 1993: An XCP user's guide and reference manual. Applied Physics Laboratory Tech. Rep. APL-UW TR9309, University of Washington, Seattle, WA, 59 pp. [Available from APL, University of Washington, 1013 NE 40th St., Seattle, WA 98105-6698.]
- Schmitt, R. W., J. M. Toole, R. L. Koehler, E. C. Mellinger, and K. W. Doherty, 1988: The development of a fine- and microstructure profiler. *J. Atmos. Oceanic Technol.*, **5**, 484–500.
- Sjöberg, B., and A. Stigebrandt, 1992: Computations of the geographical distribution of the energy flux to mixing processes via internal tides and the associated vertical circulation in the ocean. *Deep-Sea Res.*, **39**, 269–291.
- Slinn, D. N., and J. J. Riley, 1996: Turbulent mixing in the oceanic boundary layer caused by internal wave reflection from sloping terrain. *Dyn. Atmos. Oceans*, **24**, 51–62.
- Smith, W. H. F., and D. T. Sandwell, 1997: Global sea floor topography from satellite altimetry and ship depth soundings. *Science*, **277**, 1956–1962.
- St. Laurent, L., and C. Garrett, 2002: The role of internal tides in mixing the deep ocean. *J. Phys. Oceanogr.*, **32**, 2882–2899.
- , H. L. Simmons, and S. R. Jayne, 2002: Estimating tidally driven mixing in the deep ocean. *Geophys. Res. Lett.*, **29**, 2106, doi: 10.1029/2002GL015633.
- , S. Stringer, C. Garrett, and D. Perrault-Joncas, 2003: The generation of internal tides at abrupt topography. *Deep-Sea Res.*, **50**, 987–1003.
- Tarbell, S. A., E. T. Montgomery, and M. G. Briscoe, 1985: A compilation of moored current meter and wind recorder data, Volume VIII, Long-Term Upper Ocean Study (LOTUS): (Moorings 787, 788, 789, 790, 792) April 1983–May 1984. Woods Hole Oceanographic Institution Tech. Rep. 85-39, 186 pp.
- Thorpe, S. A., 1987: On the reflection of a train of finite-amplitude internal waves from a uniform slope. *J. Fluid Mech.*, **178**, 279–302.
- , 1992: The generation of internal waves by flow over the rough topography of a continental slope. *Proc. Roy. Soc. London*, **439A**, 115–130.
- , 2001: Internal wave reflection and scatter from sloping rough topography. *J. Phys. Oceanogr.*, **31**, 537–553.
- Toole, J. M., R. W. Schmitt, K. L. Polzin, and E. Kunze, 1997: Near-boundary mixing above the flanks of a midlatitude seamount. *J. Geophys. Res.*, **102** (C1), 947–959.
- Wesson, J. C., and M. C. Gregg, 1994: Mixing at Camarinal Sill in the Strait of Gibraltar. *J. Geophys. Res.*, **99** (C5), 9847–9878.
- Wunsch, C., 1969: Progressive internal waves on slopes. *J. Fluid Mech.*, **35**, 131–144.
- , 1975: Internal tides in the ocean. *Rev. Geophys.*, **13**, 167–182.
- Zervakis, V., E. Krasakopoulou, D. Georgopoulos, and E. Souvermezoglou, 2003: Vertical diffusion and oxygen consumption during stagnation periods in the deep North Aegean. *Deep-Sea Res.*, **50**, 53–71.